JAMES | Journal of Advances in Modeling Earth Systems

RESEARCH ARTICLE
10.1029/2020MS002116

Key Points:
- Fine-scale flow-vegetation interactions can considerably impact large-scale biogeomorphic feedbacks
- Current large-scale biogeomorphic models are too coarse to include these fine-scale interactions
- Our computationally efficient method allows large-scale models to account for fine-scale interactions

Supporting Information:
- Supporting Information S1

Correspondence to:
O. Gourgue,
ogourgue@gmail.com

Citation:
Gourgue, O., van Belzen, J., Schwarz, C., Bouma, T. J., van de Koppel, J., & Temmerman, S. (2020). A convolution method to assess subgrid-scale interactions between flow and patchy vegetation in biogeomorphic models. *Journal of Advances in Modeling Earth Systems*, *12*, e2020MS002116. https://doi.org/10.1029/2020MS002116

Received 19 MAR 2020
Accepted 5 SEP 2020
Accepted article online 11 SEP 2020

A Convolution Method to Assess Subgrid-Scale Interactions Between Flow and Patchy Vegetation in Biogeomorphic Models

Olivier Gourgue[1,2], Jim van Belzen[3,1], Christian Schwarz[4], Tjeerd J. Bouma[3], Johan van de Koppel[3,5], and Stijn Temmerman[1]

[1]Ecosystem Management Research Group, University of Antwerp, Antwerp, Belgium, [2]Department of Earth and Environment, Boston University, Boston, MA, USA, [3]Department of Estuarine and Delta Systems, and Utrecht University, NIOZ Royal Netherlands Institute for Sea Research, Yerseke, Netherlands, [4]College of Earth, Ocean and Environment, University of Delaware, Newark, DE, USA, [5]Conservation Ecology Group, Groningen Institute for Evolutionary Life Sciences, University of Groningen, Groningen, Netherlands

Abstract Interactions between water flow and patchy vegetation are governing the functioning of many ecosystems. Yet, numerical models that simulate those interactions explicitly at the submeter patch scale to predict geomorphological and ecological consequences at the landscape scale (order of km^2) are still very computationally demanding. Here, we present a novel and efficient convolution technique to incorporate biogeomorphic feedbacks in numerical models across multiple spatial scales (from less than 1 m^2 to several km^2). This new methodology allows for spatially refining coarse-resolution hydrodynamic simulations of flow velocities (order of m) around fine-resolution patchy vegetation patterns (order of 10 cm). Although flow perturbations around each vegetation grid cell are not simulated with the same level of accuracy as with more expensive finer-resolution models, we show that our approach enables spatial refinement of coarse-resolution hydrodynamic models by resolving efficiently subgrid-scale flow velocity patterns within and around vegetation patches (mean error, spatial variability, and spatial correlation improved by, respectively, 13%, 66%, and 49% on average in our test cases). We also provide evidence that our approach can substantially improve the representation of important biogeomorphic processes, such as subgrid-scale effects on net sedimentation rate and habitable surface area for vegetation (respectively 66% and 39% better on average). Finally, we estimate that replacing a fine-resolution model by a coarser-resolution model associated with the convolution method could reduce the computational time of real-life fluctuating flow simulations by several orders of magnitude. This marks an important step forward toward more computationally efficient multiscale biogeomorphic modeling.

Plain Language Summary The functioning of many ecosystems, such as rivers, wetlands, and shallow seas, is governed by the interactions between water flow and small patches of vegetation. Powerful tools to investigate the formation and evolution of these ecosystems are computer programs that split the study area into different grid cells on which fundamental equations of water movement are solved. However, these programs (so-called numerical models) necessitate a lot of computational power, as they require fine grid resolutions (a lot of small grid cells) to account for small patches of vegetation. In this paper, we present a new approach where the fundamental equations are solved at relatively coarse resolution (few large grid cells of tens of square meters). The water flow patterns are then recalculated at finer resolution (smaller grid cells of less than 1 m^2) with a novel technique that requires only little computational power (so-called convolution method). By comparing with laboratory measurements and the results from a numerical model at much finer resolution (grid cells of a few square centimeters), we provide evidence that this approach is a good compromise between accuracy and computational time, hence allowing to study the formation and evolution of large ecosystems with more extensive details.

1. Introduction

Over the last two decades, it has become increasingly clear that two-way interactions between biological and physical processes, so-called biogeomorphic feedbacks, play a key role in the formation and evolution of many landscapes (Corenblit et al., 2015; Murray et al., 2008; Reinhardt et al., 2010). In recent years, it has

been highlighted more specifically that the interactions between water flow and the aboveground biomass of small-scale vegetation patches (order of m^2) govern the formation and evolution of landform and vegetation patterns at the landscape scale (order of km^2 Folkard, 2019; Larsen, 2019). For example, in alluvial rivers (Figure 1a), pioneer islands induced by vegetation patches, sometimes in association with dead wood, facilitate the establishment of other plants that can in turn reinforce the development of larger vegetated landforms (Francis et al., 2009; Gurnell, 2014). In lowland rivers (Figure 1b), patches of macrophytes affect the spatial patterns of water flow, sedimentation, and erosion at river reach scales, facilitating the further establishment and growth of adjacent macrophytes (Schoelynck et al., 2012) and promoting biodiversity (Cornacchia et al., 2018). In freshwater marshes (Figure 1c), feedbacks between flow, sediment redistribution, vegetation dynamics, and peat accretion lead to regular flow-parallel patterning of ridges and sloughs (Bernhardt & Willard, 2009; Heffernan et al., 2013; Larsen et al., 2007). In tidal salt marshes (Figure 1d), expanding patches of pioneer vegetation trigger the formation of dense, efficient drainage channel networks (Kearney & Fagherazzi, 2016; Schwarz et al., 2018; Taramelli et al., 2018; Temmerman et al., 2007; Vandenbruwaene et al., 2015). In seagrass beds (Figure 1e), patchiness controls the spatial distribution of shear stress, suspended sediment, light environment, and consequent seagrass habitat suitability (Carr et al., 2016; van der Heide et al., 2010). In river basins, vegetation patterns resulting from the interplay between climate, soils, and topography in turn exert important controls on the hydrologic and geomorphic processes that contribute to the formation of landscape morphology over the long term (Istanbulluoglu & Bras, 2005; Nakayama, 2012; Saco et al., 2007). While theory on such biogeomorphic landscape formation is now widely adopted, numerical process-based models that integrate patch-scale (order of m^2) vegetation-flow interactions with their impact on landscape-scale (order of km^2) biomorphodynamics are still computationally very demanding (Le Hir et al., 2007) and hence limited to small-scale, simple-geometry cases (e.g., Carr et al., 2016; Crosato & Saleh, 2011; de Lima et al., 2015; Larsen et al., 2017; Schwarz et al., 2014; Yamasaki et al., 2019, for the ecosystems mentioned above). Alternative options at the landscape scale include empirical cellular automata (e.g., Fonstad, 2006; Larsen & Harvey, 2011; Murray & Paola, 2003) and process-based models that consider vegetation as a large homogeneous, nonpatchy continuum (e.g., Belliard et al., 2015; D'Alpaos et al., 2007; Sandi et al., 2018, for tidal salt marshes) which fail at representing small-scale feedbacks critical for habitat structure.

In general, the establishment of vegetation in an initially bare landscape modifies the patterns of water flow, sedimentation, and erosion, which in return influences the spatial patterns of vegetation establishment and die-off (Piliouras & Kim, 2019). In case of patchy vegetation, these biogeomorphic feedbacks are scale dependent. At a small scale, within the vegetation patches, flow velocities and erosion are reduced (e.g., Nepf, 2012) resulting in improved plant growth (positive feedback van Wesenbeeck et al., 2008). At a larger scale, the water is partly forced to flow around the vegetation patches, leading there to increased flow velocities (Zong & Nepf, 2010), potential erosion (Bouma et al., 2007), and to inhibition of plant growth just next to the vegetation patch (negative feedback van Wesenbeeck et al., 2008). Scale-dependent biogeomorphic feedbacks have been studied extensively over the past decade. Their strength is reported to depend on many characteristics, such as patch size (Licci et al., 2019; Vandenbruwaene et al., 2011), stem density (Bouma et al., 2009), stem height (Gu et al., 2018), stem stiffness (Bouma et al., 2013; Marjoribanks et al., 2019; Ortiz et al., 2013; Schwarz et al., 2015), interpatch distance (de Lima et al., 2015; Meire et al., 2014; Vandenbruwaene et al., 2011), lateral expansion rate (Schwarz et al., 2018), and flow velocity (Bouma et al., 2013; Marjoribanks et al., 2019; Vandenbruwaene et al., 2011). Several studies have also shown that strong scale-dependent feedbacks are needed to result in the self-organization of regular spatial biogeomorphic patterns at the landscape scale (Rietkerk et al., 2004; Schwarz et al., 2018; Temmerman et al., 2007; van de Koppel et al., 2012). Given the above description of the scale dependency of biogeomorphic feedbacks, it becomes evident that their representation within numerical models is highly dependent on the grid size, which raises a balance problem between domain size and computational time. For instance, grid cells that are small enough to allow for representing biogeomorphic processes across all necessary spatial scales could result in simulations not running faster than real time for large domain sizes. Traditional process-based models therefore need new computationally efficient methodologies to account for detailed representation of the small-scale interactions between vegetation patches and their environment. This is crucial to enable the explicit simulation of patch-scale biogeomorphic feedbacks and their impact at the landscape scale.

In this study, we present and evaluate a novel convolution method that enables to account for subgrid-scale interactions between water flow and vegetation patches in large-scale coarse-resolution biogeomorphic

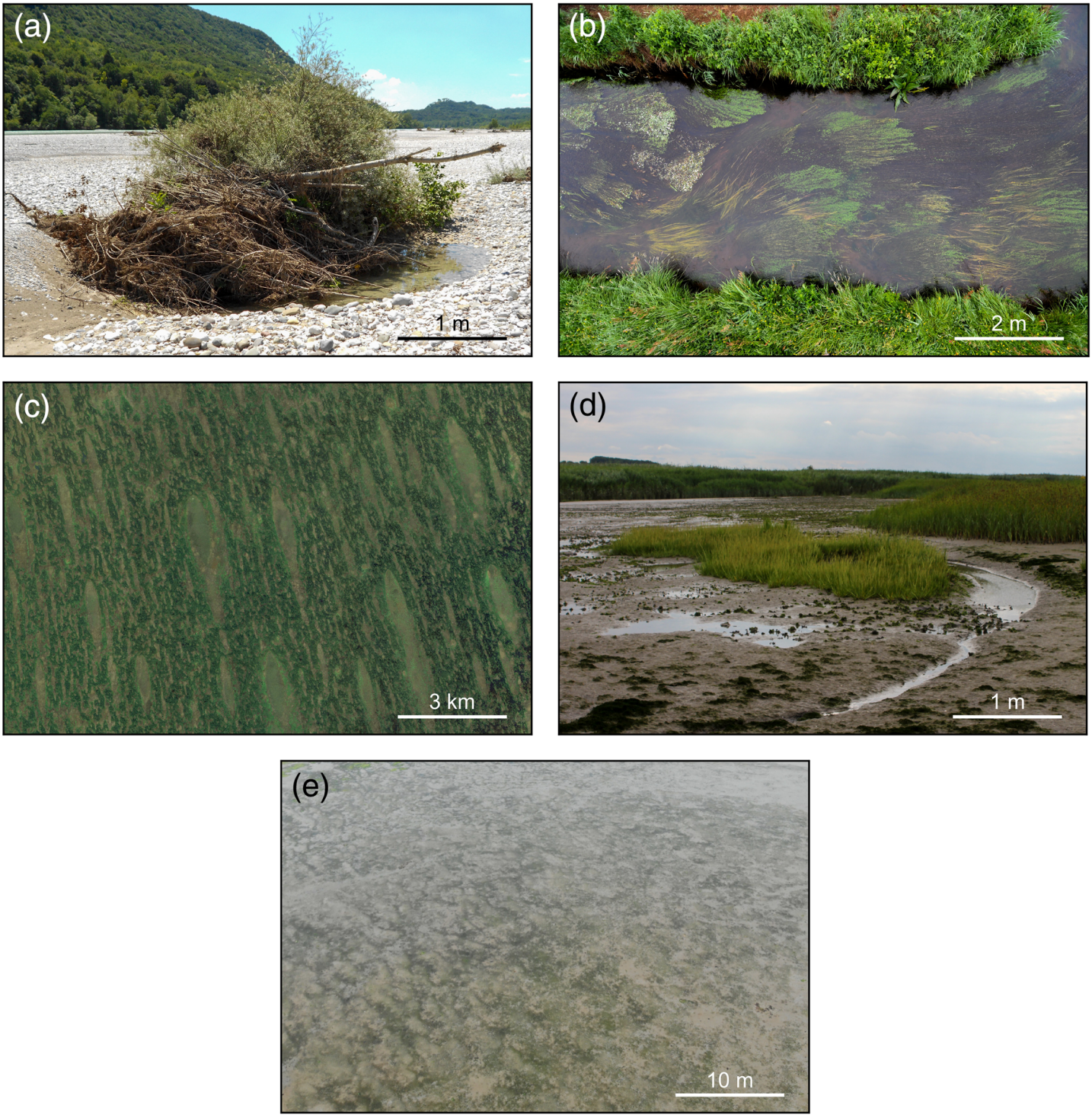

Figure 1. (a) Example of pioneer island in an alluvial river, Tagliamento river, Italy (photograph by Angela Gurnell). (b) Example of macrophyte patches in a lowland river, Desselse Nete river, Belgium (orthogonal photograph from a pole by Kerst Buis and Jonas Schoelynck). (c) Example of ridge and slough landscape in a freshwater marsh, Everglades, FL, United States (photograph from Google Earth). (d) Example of expanding vegetation patch in a tidal salt marsh, Sieperdaschor, the Netherlands (photograph by Olivier Gourgue). (e) Example of patchiness in a seagrass bed, Eastern Scheldt, the Netherlands (oblique photograph from a drone by Klaas van de Ketterij). Scales are only indicative.

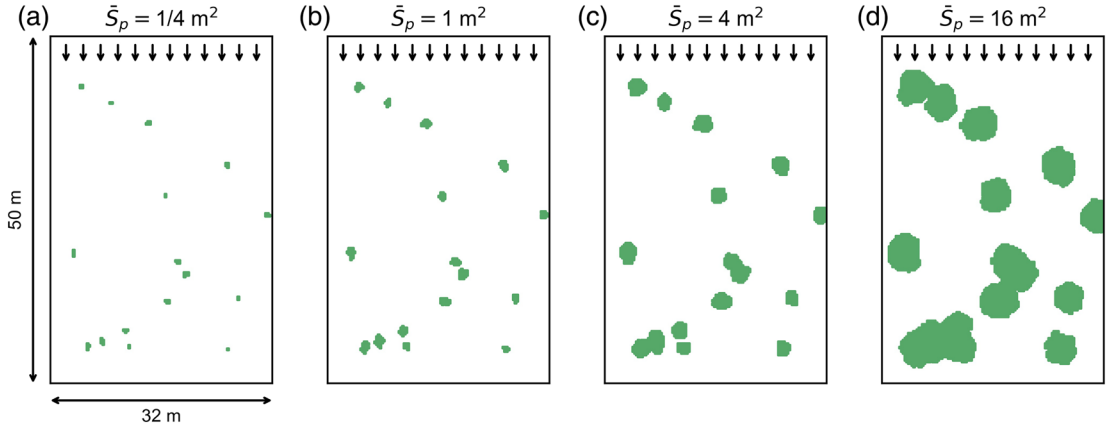

Figure 2. Example of 16 randomly distributed vegetation patches (green plots) with a mean patch surface area $\bar{S}_p = 1/4\,\mathrm{m}^2$ (a), $1\,\mathrm{m}^2$ (b), $4\,\mathrm{m}^2$ (c), and $16\,\mathrm{m}^2$ (d). The single-headed arrows indicate the incoming flow direction. The double-headed arrows indicate the domain dimensions.

models, without affecting their computational efficiency. We demonstrate and evaluate the method for the case of patchy vegetation in tidal salt marsh systems, focusing on the interactions between water flow and static vegetation patches. The novelty of the method is that we adopt a hybrid approach in which flow velocities are first simulated at coarse resolution using a traditional process-based model, while vegetation is represented at a much finer subgrid-scale resolution. Flow velocities are then interpolated at the subgrid scale using a very efficient convolution method. Doing so, we keep computational resources at a reasonable level, while for the first time allowing to account for flow interactions with smaller vegetation patches than the hydrodynamic model grid size.

2. Methods

2.1. Conceptual Study Design

In this study, we focus on the interactions between water flow and randomly distributed vegetation patches of different sizes in a simple rectangular domain with unidirectional flow (Figure 2; more details in section 2.5.3). We use three different modeling approaches to simulate these interactions:

1. The Standard-Resolution Model (SRM) is a process-based model that solves the shallow water equations (section 2.3) on relatively coarse 5-m-resolution unstructured grids (Figure 3a). With such a grid resolution, SRM is representative of today's state-of-the-art two-dimensional tidal-marsh biogeomorphic models (e.g., Belliard et al., 2015; Best et al., 2018; Bij de Vaate et al., 2020; Brckner et al., 2019; Mariotti, 2018;

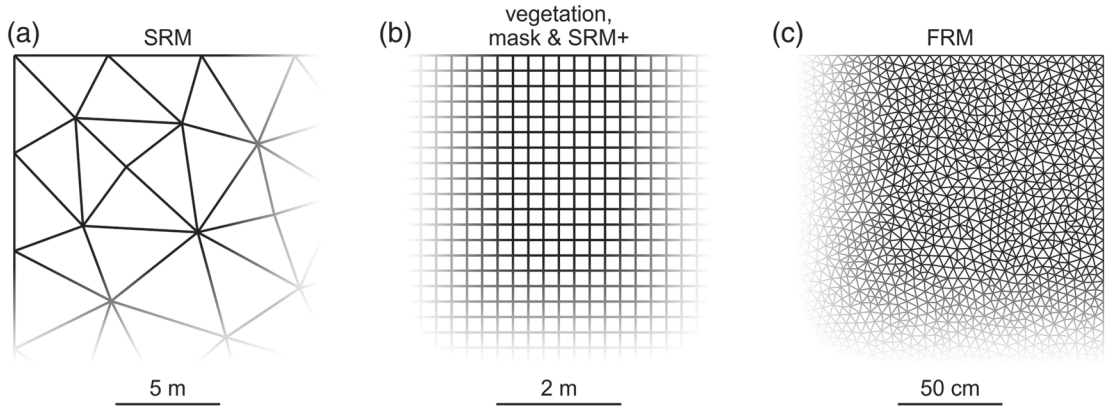

Figure 3. Example of computational grids used with the different modeling approaches. (a) The Standard-Resolution Model (SRM) uses 5-m-resolution unstructured triangular grids. (b) The spatially refined Standard-Resolution Model (SRM+) uses 25-cm-resolution structured rectangular grids on which the vegetation and the convolution mask are also defined. (c) The Fine-Resolution Model (FRM) uses 5-cm-resolution triangular grids. For illustration purposes, different scales are used in each subfigure.

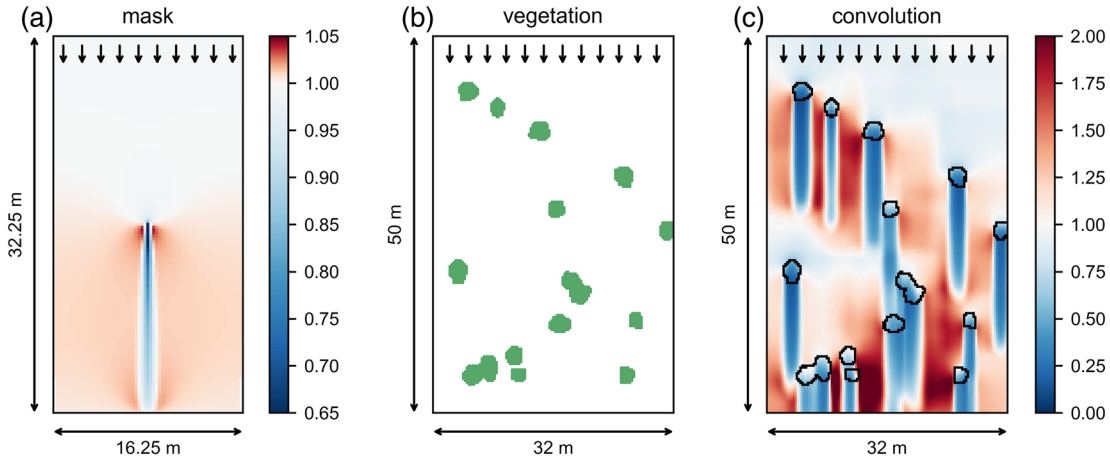

Figure 4. Illustration of the main variables involved in the convolution method (Equation 9). (a) The convolution mask (M) is the magnitude of the normalized flow velocity around an elementary 25-by-25-cm vegetation patch located in the center of the domain, as simulated by FRM, projected on a 25-cm-resolution rectangular grid (Figure 3b) and normalized by division of the simulated flow field by the incoming velocity (more details in section 2.5.2). (b) The vegetation is defined on a 25-cm-resolution rectangular grid (Figure 3b), here illustrated with an example of 16 randomly distributed vegetation patches (green plots) with a mean patch surface area of 4 m^2. (c) The magnitude of the normalized flow velocities (U/U_0) resulting from the convolution method is defined on the same grid as the vegetation distribution (Figure 3b). The black polygons indicate the contours of the vegetation patches. The single-headed arrows indicate the incoming flow direction. The double-headed arrows indicate the different domain dimensions.

Sandi et al., 2018; Schwarz et al., 2014; Zhang et al., 2019), which by definition are unable to represent fine-scale interactions between flow and small vegetation patches (order of m^2) and hence their biogeomorphic impacts at the landscape scale (order of km^2).

2. The spatially refined Standard-Resolution Model (SRM+) is at the core of this study. Using a novel convolution method (section 2.2), we spatially refine SRM flow velocities on 25-cm-resolution structured grids (Figure 3b) on which the vegetation distribution is also defined. As convolution algorithms are very well optimized, the increase of computational time due to our spatial refinement methodology is marginal.
3. The Fine-Resolution Model (FRM) is very similar to SRM, except that it uses much finer 5-cm-resolution unstructured grids (Figure 3c). With such a fine grid resolution, FRM is very computationally expensive. However, it is calibrated against flume measurements (section 2.5.1) and can provide reference solutions on small-scale simple-geometry cases to assess the performance of our new modeling approach.

2.2. Convolution Method

2.2.1. Conceptual Approach

The main assumption supporting our new convolution method is that the flow velocities around complex vegetation patterns can be approximated by combining the impact that single elementary vegetation units would have separately on the flow. The convolution mask (Figure 4a) is the magnitude of the normalized flow velocity around an elementary vegetation patch of the size of one single vegetation grid cell (i.e., 25 by 25 cm) simulated at 5-cm resolution with FRM (more details in section 2.5.2). It can be regarded as the spatially explicit matrix describing the flow perturbation around one single elementary vegetation grid cell. Our main assumption is that the magnitude of the flow velocity around more complex vegetation patterns (i.e., consisting of multiple vegetation grid cells like in Figure 4b) can be approximated by combining the flow perturbation (i.e., the convolution mask) around each individual elementary vegetation grid cell. Practically, we start from a homogeneous flow field defined on the vegetation grid, which we multiply iteratively by the convolution mask around each individual vegetated grid cell. That is, for each vegetated grid cell, we multiply iteratively the flow velocity by the convolution mask over an area centered on the vegetated grid cell and of the size of the convolution mask. The final result is a combination of the cumulative effect of each individual vegetated grid cell obtained through multiplication of each individual convoluted flow field, which approximates the flow velocities around the complex patchy vegetation distribution (Figure 4c).

The convolution method works on the structured vegetation grid (Figure 3b). The magnitude of the flow velocity, the convolution mask, and the vegetation distribution can therefore be represented by two-dimensional matrices, namely, U, M, and V. Each element of these matrices corresponds to a value of the corresponding variable on a rectangular grid with the same resolution as the vegetation grid. While the

velocity and vegetation matrices are of the same size as the vegetation grid, the size of the mask matrix is different. Its indices vary from $-K$ to K in the x direction and from $-L$ to L in the y direction, while K and L determine the size of the convolution mask (section 2.5.2). The single vegetated cell of the convolution mask is centered on indices $(0, 0)$. Following our main assumption, the magnitude of the flow velocity can be approximated as follows:

$$U_{i,j} = U_0 \prod_{k=-K}^{K} \prod_{l=-L}^{L} {M_{k,l}}^{V_{i-k,j-l}}, \tag{1}$$

where U_0 is the incoming flow velocity, and $V_{i,j} = 1$ on vegetated grid cells and 0 elsewhere. The use of normalized flow velocities for the convolution mask, which are then rescaled by U_0 in Equation 1, is justified by flume experiments, where no significant differences were noticed in the relative increase and decrease of flow velocities around vegetation patches for different incoming flow velocities (Vandenbruwaene et al., 2011).

At this point, it is important to highlight that the right-hand side of Equation 1 presents remarkable similarities with the two-dimensional discrete convolution of two matrices F and G:

$$F_{i,j} \ast\ast G_{i,j} = \sum_{k=-K}^{K} \sum_{l=-L}^{L} F_{k,l} G_{i-k,j-l}. \tag{2}$$

By taking the exponential of both sides, we can convert the double sum sequence into a double product sequence:

$$\exp\left(F_{i,j} \ast\ast G_{i,j}\right) = \exp\left(\sum_{k=-K}^{K} \sum_{l=-L}^{L} F_{k,l} G_{i-k,j-l}\right), \tag{3}$$

$$= \prod_{k=-K}^{K} \prod_{l=-L}^{L} \exp\left(F_{k,l} G_{i-k,j-l}\right). \tag{4}$$

Let $F = \log(M)$ and $G = V$. Equation 4 then becomes

$$\exp\left(\log\left(M_{i,j}\right) \ast\ast V_{i,j}\right) = \prod_{k=-K}^{K} \prod_{l=-L}^{L} \exp\left(\log\left(M_{k,l}\right) V_{i-k,j-l}\right), \tag{5}$$

$$= \prod_{k=-K}^{K} \prod_{l=-L}^{L} \exp\left(\log\left({M_{k,l}}^{V_{i-k,j-l}}\right)\right), \tag{6}$$

$$= \prod_{k=-K}^{K} \prod_{l=-L}^{L} {M_{k,l}}^{V_{i-k,j-l}}. \tag{7}$$

Finally, by combining Equations 1 and 7, we can simply write

$$U_{i,j} = U_0 \exp\left(\log\left(M_{i,j}\right) \ast\ast V_{i,j}\right). \tag{8}$$

From a strictly mathematical point of view, Equations 1 and 8 are equivalent. From a more practical, computational point of view, they are, however, very different. On the one hand, implementing Equation 1 as is would lead to a computationally inefficient four-nested-loop structure. On the other hand, with Equation 8, we can take advantage of existing libraries that compute convolution products very efficiently by resorting to the convolution theorem. The latter states that, under suitable conditions, the Fourier transform of the convolution of two signals is the pointwise product of their Fourier transforms. In this study, we use the open source module *fftconvolve* from the Python package *SciPy* (Virtanen et al., 2019). In what follows, in order to simplify the notation and improve readability, we write Equation 8 and subsequent developments without grid cell indices:

$$U = U_0 \exp\left(\log(M) \ast\ast V\right). \tag{9}$$

The result of the convolution method depends greatly on the convolution mask itself. That is why the latter is here generated at fine resolution (5 cm) with a numerical model calibrated against flume measurements (section 2.5.2) before being projected at the final, coarser resolution of 25 cm. Also, the mask dimensions have an impact and must be chosen to balance model performance with computational cost. They are here defined to correspond as much as possible to the flume experimental setup in terms of distance between vegetation patches and lateral and outlet boundaries, with the additional constraint that the convolution mask must fit a 25-by-25-cm vegetation patch at the center of its grid. The resulting design proves to be quite optimal for our study cases (supporting information Figure S1).

Preliminary tests have shown that our approach allows for qualitatively good representation of the flow perturbation patterns around vegetation patches. However, using Equation 1 or 8 as is leads to considerable overestimation of the flow perturbation intensity, which grows with the size of surrounding vegetation patches (supporting information Text S1 and Figures S2 and S3). This is solved by rescaling the vegetation matrix V to account for the vegetation surface within the area of influence of the convolution mask:

$$U = U_0 \exp\left(\log(M) \ast\ast \hat{V}\right), \tag{10}$$

where $\hat{V}$ is the rescaled vegetation matrix

$$\hat{V} = \frac{V}{\left((V \ast\ast J)(\Delta x)^2\right)^{\beta}}, \tag{11}$$

where J is an all-ones matrix of the same size as M and with inverse dimensions of a surface, Δx is the vegetation grid size, and β is a dimensionless calibration parameter. The optimal value of β for this study is 0.5 (supporting information Text S2 and Figures S4 and S5).

2.2.2. Practical Implementation

The conceptual approach (section 2.2.1) is restricted to cases with unidirectional steady flows. This may be suitable in simple cases with small vegetation patches, for which the flow directions are barely affected. However, this is not appropriate for applications to systems with spatially varying flow directions, such as meandering channels or tidal environments. In this section, we describe a practical implementation of the convolution method for such complex systems in steady state conditions (see supporting information Text S3 and Figure S6 for transposition to fluctuating flow regimes) starting from flow velocities simulated at relatively coarse resolution with SRM (Figures 5a and 5b) which are then spatially refined following a four-step methodology.

2.2.2.1. Step 1: Conceptual Approach Applied in N_θ Directions

We first apply a normalized version of the conceptual approach in N_θ different directions θ_i (Figures 5d to 5f). That is, we rotate the convolution mask M so that the background flow is oriented along θ_i, and we apply Equation 10 with $U_0 = 1$:

$$U'_{\theta_i} = \exp\left(\log\left(M_{\theta_i}\right) \ast\ast \hat{V}\right) \text{ for } i = 1, \ldots, N_\theta, \tag{12}$$

where U'_{θ_i} is the normalized convoluted velocity matrix in the ith direction θ_i, and M_{θ_i} is the mask matrix rotated along the ith direction θ_i. Doing so, we generate N_θ directional maps on the vegetation grid (i.e., each vegetation grid cell has N_θ potential values U'_{θ_i}, depending on the direction of the background flow θ_i). Typically, but not necessarily, we use $N_\theta = 8$ for the cardinal (N, E, S, and W) and intercardinal directions (NE, SE, SW, and NW).

2.2.2.2. Step 2: Aggregation of Directional Maps

We use SRM flow directions (Figure 5b) and Voronoi clusters (Figure 5c) to select the appropriate values of U'_{θ_i} on each vegetation grid cell (Figure 5g). A Voronoi cluster is made up of all the vegetation grid cells that are closer to a specific SRM grid node than any other SRM grid node. Each Voronoi cluster is associated with the flow direction θ_{SRM} on the corresponding SRM grid node. Within each Voronoi cluster, we select the values of U'_{θ_i} from the directional map corresponding to the direction θ_i that is the closest to θ_{SRM}:

$$U' = \sum_{i=1}^{N_\theta} U'_{\theta_i} f_i(\theta_{SRM}), \tag{13}$$

where U' is the normalized aggregated velocity matrix, and f_i is an indicator function, which is equal to 1 for θ_i such that $|\theta_{SRM} - \theta_i|$ is minimum, and 0 otherwise.

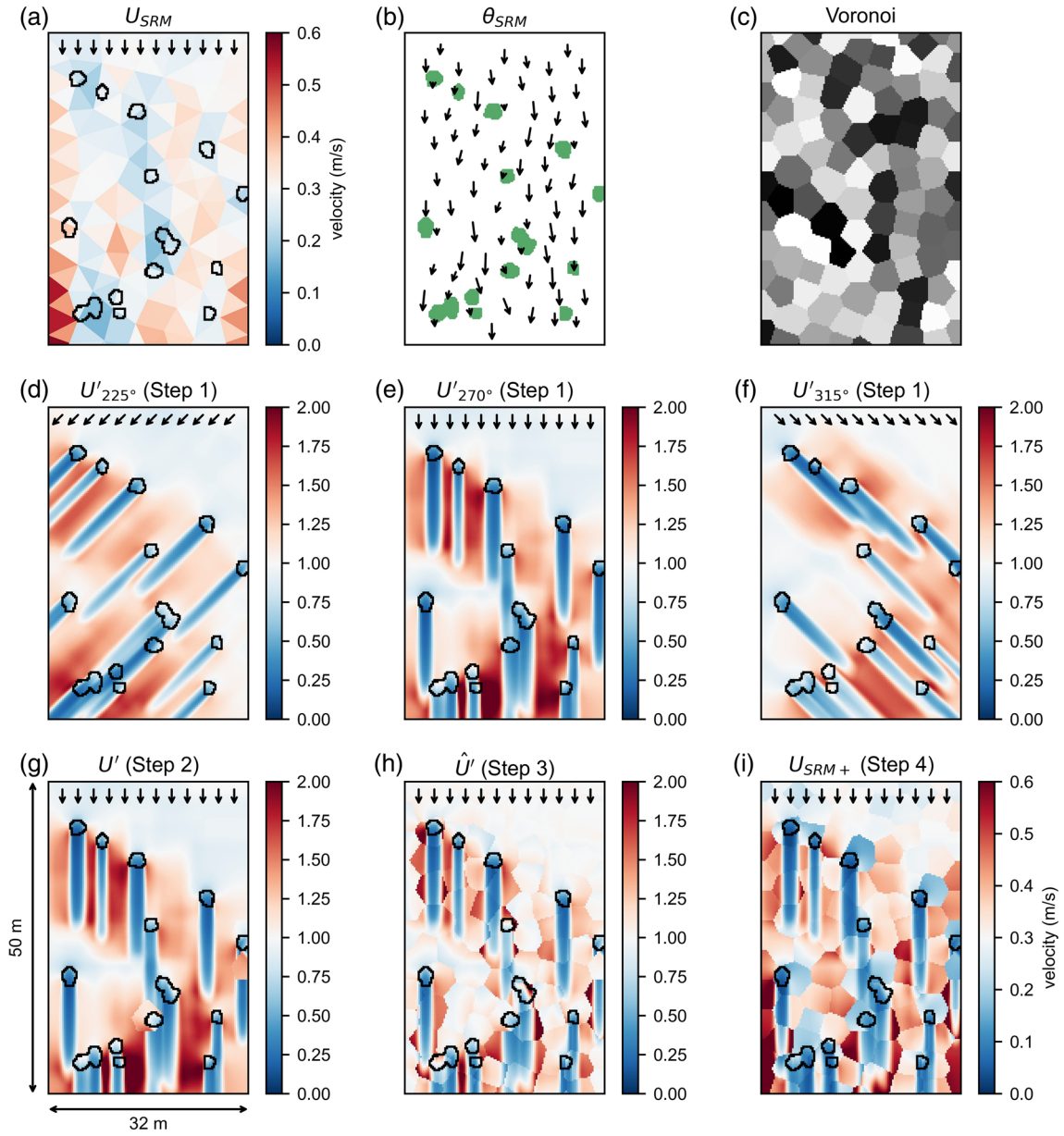

Figure 5. Illustration of the different steps of the convolution method applied to complex systems with spatially varying flow directions (example of 16 randomly distributed vegetation patches—black polygons or green plots—with a mean patch surface area of 4 m^2). (a) Magnitude and (b) direction of the flow velocities simulated by SRM. (c) Illustration of the concept of Voronoi clusters (different shades of gray) which are made up of all the vegetation grid cells (Figure 3b) that are closer to one specific SRM grid node (Figure 3a) than any other SRM grid node. (d–f) Normalized convoluted velocity matrix (Step 1) along three directions ($\theta = 225°$, 270°, and 315°). (g) Normalized aggregated velocity matrix (Step 2). (h) Normalized conservative velocity matrix (Step 3). (i) Spatially refined velocity matrix (Step 4). The single-headed arrows indicate the incoming (a, d–i) or local (b) flow directions. The double-headed arrows indicate the domain dimensions.

2.2.2.3. Step 3: Conservation of Momentum

To prevent any creation of momentum by the convolution method itself, the normalized aggregated flow field U' is rescaled by its mean value within each Voronoi cluster $\overline{U'}_{vor}$ (Figure 5h):

$$\hat{U}' = \frac{U'}{\overline{U'}_{vor}}, \tag{14}$$

where $\hat{U}'$ is the normalized conservative velocity matrix. With this step, we guarantee that the convolution method serves only as a redistribution of flow velocities within a Voronoi cluster and hence that the overall momentum is conserved over the entire domain.

2.2.2.4. Step 4: Spatial Refinement

Finally, within each Voronoi cluster, the normalized conservative velocity matrix $\hat{U}'$ is simply multiplied by the magnitude of the flow velocity on the corresponding SRM grid node U_{SRM} (Figure 5i):

$$U_{SRM+} = U_{SRM}\hat{U}', \tag{15}$$

where U_{SRM+} is the spatially refined velocity matrix.

2.3. Process-Based Models (SRM and FRM)

The convolution method is in principle compatible with any process-based hydrodynamic model. Here, however, we use the finite element solver suite Telemac to perform numerical simulations of the flow around vegetation patches. More specifically, we use the module Telemac-2D, which solves the depth-averaged shallow water equations in a two-dimensional horizontal framework (Hervouet, 2007)

$$\frac{\partial h}{\partial t} + \boldsymbol{\nabla}\cdot(h\boldsymbol{u}) = 0, \tag{16}$$

$$\frac{\partial \boldsymbol{u}}{\partial t} + \boldsymbol{u}\cdot\boldsymbol{\nabla}\boldsymbol{u} = -g\boldsymbol{\nabla}\eta + \frac{1}{h}\boldsymbol{\nabla}\cdot(h\nu\boldsymbol{\nabla}\boldsymbol{u}) - \frac{\boldsymbol{\tau}_b + \boldsymbol{\tau}_v}{\rho h}, \tag{17}$$

where h is the water depth, t is the time, $\boldsymbol{\nabla}$ is the differential operator, $\boldsymbol{u}$ is the depth-averaged water flow velocity, $g = 9.81\,\mathrm{m/s^2}$ is the gravitational acceleration, η is the water surface elevation above a reference level, ν is the diffusion coefficient, $\boldsymbol{\tau}_b$ is the bed shear stress, $\boldsymbol{\tau}_v$ is the vegetation resistance force per unit horizontal area, and $\rho = 1{,}000\,\mathrm{kg/m^3}$ is the water density.

The diffusion coefficient ν is computed using the standard $k-\epsilon$ turbulence model (Launder & Spalding, 1974) and the bed shear stress with the classical Manning formula:

$$\boldsymbol{\tau}_b = \frac{\rho g n^2}{h^{1/3}}\|\boldsymbol{u}\|\boldsymbol{u}, \tag{18}$$

where the Manning coefficient n is empirically derived and depends mainly on surface roughness. We use here a value of $0.013\,\mathrm{s/m^{1/3}}$, which is typical for concrete channels like in the original flume experiments used for the model calibration (section 2.5.1).

The vegetation resistance force is modeled as the drag force on a random or staggered array of rigid cylinders with uniform properties. To simplify the equations and focus on readability, we only consider emerged vegetation here, even though both emerged and submerged cases can be represented with such a model (Baptist et al., 2007). The equivalent shear stress due to vegetation drag therefore reads

$$\boldsymbol{\tau}_v = \frac{1}{2}\rho C_d m d h\|\boldsymbol{u}\|\boldsymbol{u}, \tag{19}$$

where C_d is the bulk drag coefficient, m is the number of stems per unit horizontal area, and d is the stem diameter. The bulk drag coefficient C_d is a parameter difficult to determine as it cannot be measured directly. In principle, its value for smooth cylinders is known from experimental studies and theory, and it depends on the Reynolds number and the spatial arrangement of the cylinders (Vogel, 1996). In practice, it is often used as a calibration parameter, in an effort to account for complex properties of real plants (Baptist et al., 2007). In this study, we calibrate the bulk drag coefficient using flume experiment measurements on flow interactions with patches of *Spartina anglica* (section 2.5.1). Consistently with the flume study, we use a density of 658 stems/m^2 and a stem diameter of 3 mm (Bouma et al., 2013; Vandenbruwaene et al., 2011).

Using the finite element method, Telemac solves the shallow water equations on unstructured triangular grids. In this study, we set up two different models (SRM and FRM) using, respectively, 5-m (Figure 3a) and 5-cm grid resolutions (Figure 3c). All grids are created using the finite element mesh generator Gmsh (Geuzaine & Remacle, 2009).

The vegetation is defined on structured rectangular grids in which 25-by-25-cm cells (Figure 3b) are either fully vegetated or completely bare. As the FRM grid resolution is significantly finer than the vegetation grid (5 cm vs. 25 cm), Equation 19 can be used as is to calculate $\boldsymbol{\tau}_v$ within vegetated cells, while $\boldsymbol{\tau}_v = 0$ within bare cells. On the contrary, the SRM grid resolution is much coarser than the vegetation grid (5 m vs.

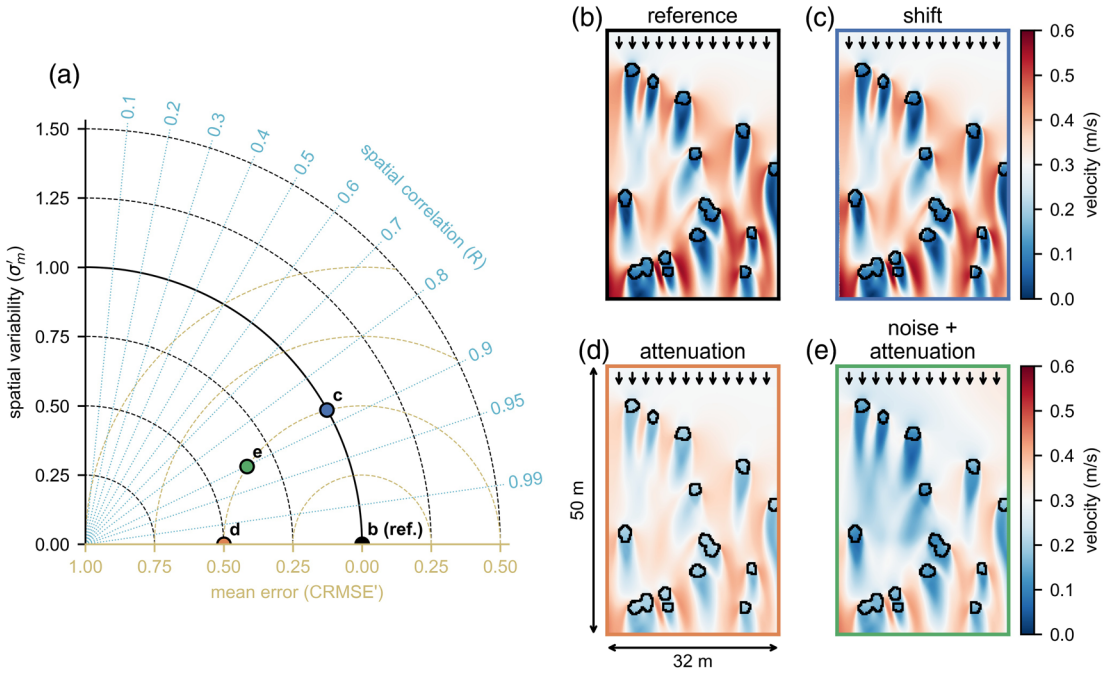

Figure 6. (a) Illustration of the concept of normalized Taylor diagram to analyze flow velocity fields around 16 vegetation patches with a mean patch surface area of 4 m^2, in comparison with a reference solution. (b) Flow velocity field simulated by FRM (reference solution). (c) Reference solution shifted by 44 cm on the right. (d) Reference solution with flow acceleration/deceleration patterns attenuated by a factor of 50%. (e) Reference solution with an additional series of Gaussian functions (with random values for the amplitude, center coordinates, and shape parameters) and with resulting flow acceleration/deceleration patterns attenuated so as to obtain $\mathrm{CRMSE}' = 0.5$. The axis colors (b–e) correspond to the marker colors in the normalized Taylor diagram (a).

25 cm). One single SRM grid node is associated with an ensemble of vegetation cells, which we call a Voronoi cluster (Figure 5c). In SRM, the right-hand side of Equation 19 is therefore multiplied by the local vegetation coverage α_{vor}, which is simply calculated as the fraction of vegetated cells within the corresponding Voronoi cluster.

All simulations in this study consist of numerical flumes in which the same constant discharge is imposed at both inlet and outlet boundaries to ensure overall mass/volume conservation. The horizontal velocity profile along the open boundaries is homogeneous. All simulations are run for 30 min, and we focus on the time-averaged flow field over the last 15 min.

2.4. Postprocessing Toolbox

With the convolution method, we do not aim at simulating details of the flow perturbations around each vegetation grid cell with the same accuracy as FRM does. Our objective is rather to efficiently refine flow velocities of SRM, at the cost of accuracy to a certain degree. With that in mind, we use Taylor diagrams (section 2.4.1) to analyze our results, as they rely on aggregated metrics (representative of the large scale) but at the same time accounting for spatial patterns in the results (representative of the subgrid scale). Our final goal is ultimately to improve the ability of SRM to quantify important biogeomorphic processes, such as the net sedimentation rate and the habitable surface area for vegetation. We also use different metrics to analyze our results from that perspective (section 2.4.2).

2.4.1. Normalized Taylor Diagrams

Taylor diagrams are polar coordinate plots that summarize multiple aspects of model performance against a reference data set in a single graph (Taylor, 2001). In their normalized version, models evaluated against different data sets can be compared in the same diagram (Kärnä & Baptista, 2016) as the underlying statistics are normalized so as to always position the reference data sets at the same spot in the diagram (see black marker "b" in Figure 6a).

Classically, Taylor diagrams and their normalized counterparts are used to analyze time series of data. Here, however, they are used to compare spatial flow velocity patterns. In a nutshell, the distance to

the reference marker indicates the mean error of the model results, while the exact location on the diagram reveals the model performance in terms of spatial variability and spatial correlation of the flow acceleration/deceleration patterns around vegetation patches. More precisely,

1. the normalized centered root mean square error CRMSE′ (yellowish circles in Figure 6a) is an indicator for good representation of the flow velocity field on average (the closer to 0 the better);
2. the normalized standard deviation σ'_m (black circles in Figure 6a) is an indicator for good representation of the spatial variability of the flow acceleration/deceleration patterns (i.e., that acceleration/deceleration patterns are simulated with the appropriate intensity—the closer to 1 the better); and
3. the correlation coefficient R (light blue lines in Figure 6a) is an indicator for good spatial correlation of the flow patterns (i.e., that acceleration/deceleration patterns are simulated at the right location—the closer to 1 the better).

In Figure 6, we illustrate the concept of normalized Taylor diagram for the specific context of this study. We look at the flow velocity field around 16 vegetation patches simulated by FRM (Figure 6b), and we compare the performance of three disturbed versions of this reference solution (Figures 6c to 6e). If the three disturbed solutions perform equally on average (CRMSE′ $= 0.5$), their quality differs in terms of spatial variability and spatial correlation of the flow acceleration/deceleration patterns. In Figure 6c, the reference solution is shifted by a few tens of centimeters. The intensity of the flow acceleration/deceleration patterns is fully conserved ($\sigma'_m = 1$) but at the expense of their spatial correlation ($R < 1$). In Figure 6d, only the intensity of the flow acceleration/deceleration patterns is altered ($\sigma'_m < 1$) so that they perfectly correlate in space with the reference solution ($R = 1$). Between those two extreme situations, we show in Figure 6e an intermediate case where both the spatial variability and the spatial correlation of the flow patterns are disturbed ($\sigma'_m < 1$ and $R < 1$). For more details on the theoretical aspects supporting normalized Taylor diagrams, we refer to Appendix A1.

2.4.2. Biogeomorphic Metrics

This study focusses primarily on the interactions between flow and vegetation, but we also want to demonstrate the potential of the convolution method in the context of biogeomorphic modeling. However, in order to keep the focus on our new methodology, we do not couple the hydrodynamic models with dynamic sediment transport and vegetation models here. Instead, we use the steady state flow velocities simulated by the three models (SRM, SRM+, and FRM) to evaluate two resulting biogeomorphic metrics: the total net sedimentation rate F_{sed} and the habitable surface area S_{hab} (i.e., the surface area where the flow conditions are suitable for potential plant growth). We then evaluate the performance of the convolution method by comparing the error made on these metrics by SRM and SRM+, using FRM as a reference.

The total net sedimentation rate is defined as

$$F_{sed} = \iint_{\Omega} (D - E)\, d\Omega, \tag{20}$$

where Ω denotes the area of interest, D is the sediment deposition rate per unit horizontal area, E is the sediment erosion rate per unit horizontal area, and $d\Omega$ is the infinitesimal element of surface area. The water-bed exchange processes are described by a combination of the so-called Partheniades and Krone's formulas, which mostly rely on the pioneer experimental work by Einstein and Krone (1962) and Partheniades (1965):

$$E = \begin{cases} M_P \left(\frac{\|\boldsymbol{\tau}_b\|}{\tau_e} - 1 \right) & \text{if } \|\boldsymbol{\tau}_b\| > \tau_e, \\ 0 & \text{otherwise,} \end{cases} \tag{21}$$

$$D = w_s C, \tag{22}$$

where M_P is the Partheniades erosion parameter, τ_e is the critical bottom shear stress for sediment erosion, w_s is the settling velocity, and C is the suspended sediment concentration. Note that we use here the continuous deposition approach in Equation 22, following the argument that the so-called critical shear stress for sediment deposition does not exist and that it rather represents a threshold for erosion of freshly deposited sediments (Winterwerp, 2007). This approach agrees with field observations in the Chesapeake Bay (Sanford & Halka, 1993) and is often adopted in recent biogeomorphic models (e.g., Adams et al., 2016; Bryan et al., 2017; Mariotti, 2018; Zhang et al., 2019, 2016). The parameter values used in our analysis ($M_P = 10^{-4}$ kg/m^{2}s,

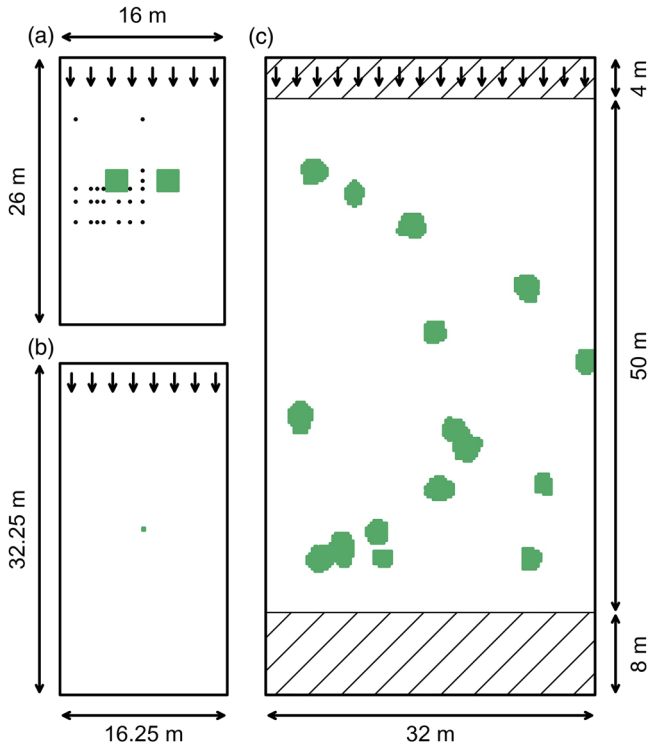

Figure 7. Schematic representation of different model scenarios considered in this study: (a) real flume experiments (section 2.5.1—here illustrated with a configuration of two square patches of 4 m^2), (b) convolution mask (section 2.5.2), and (c) randomly distributed vegetation patches (section 2.5.3—here illustrated with an example of 16 patches with a mean patch surface area of 4 m^2). The green plots represent vegetation patches. The single-headed arrows indicate the incoming flow direction. The double-headed arrows indicate the domain dimensions. The black dots indicate where flow velocities are measured in the flume experiments. The hatched areas represent inlet and outlet zones where vegetation is not present.

$\tau_e = 0.5\,\mathrm{N/m^2}$, $w_s = 4 \times 10^{-4}$ m/s, and $C = 0.1\,\mathrm{kg/m^3}$) are within typical ranges encountered in tidal salt marsh models (e.g., Belliard et al., 2015; D'Alpaos et al., 2005, 2012; Marani et al., 2007; Mariotti, 2018; Zhou et al., 2016). The relative error in total net sedimentation rate is defined as

$$\epsilon'_{sed} = \frac{\left|F_{sed} - F^{FRM}_{sed}\right|}{\left|F^{FRM}_{sed}\right|}, \tag{23}$$

where F^{FRM}_{sed} is the total net sediment rate evaluated from the reference FRM flow velocities.

The habitable surface area S_{hab} is defined as the surface area over which the flow conditions are such that $\|\boldsymbol{\tau}_b\| < \tau_v$, where τ_v is the critical bottom shear stress for vegetation growth. We use the parameter value $\tau_v = 0.26\,\mathrm{N/m^2}$ in accordance with previous biogeomorphic models for tidal salt marshes (Schwarz et al., 2014; Temmerman et al., 2007). The relative error in habitable surface area is defined as

$$\epsilon'_{hab} = \frac{\left|S_{hab} - S^{FRM}_{hab}\right|}{S^{FRM}_{hab}}, \tag{24}$$

where S^{FRM}_{hab} is the habitable surface area evaluated from the reference FRM flow velocities.

2.5. Detailed Study Design

2.5.1. Calibration of FRM Against Flume Experiments

This part expands on a former flume experimental study (Bouma et al., 2013; Vandenbruwaene et al., 2011) in which field-scale vegetation patches were placed in a large-scale 16-m-wide, 26-m-long flow facility, where a uniform, unidirectional flow was generated with 0.3 m of water depth. In most experiments, the incoming flow velocity was 0.3 m/s, which is representative of the maximal tidal currents observed on intertidal flats

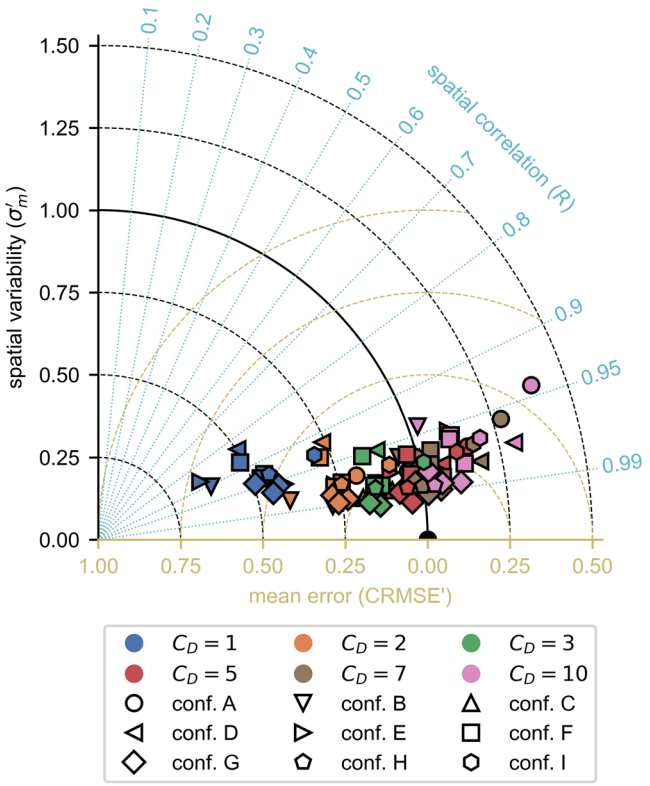

Figure 8. Normalized Taylor diagram (see explanations in section 2.4.1) comparing the performance of 78 FRM simulations with different values of the bulk drag coefficient C_d (marker colors) and for different vegetation patch configurations of the flume experiments (marker shapes). Multiple markers with the same shape and color correspond to configurations with various incoming flow velocities. The statistics are obtained by comparing simulated and observed flow velocities for the flume experiments (see section 2.5.1, Figure S7 and Table S1 for more details on the flume experiments and the different configurations).

in the Western Scheldt estuary (southwestern Netherlands) and two patches of *Spartina anglica* were placed next to each other along a cross section perpendicular to the incoming flow direction (Figure 7a). Different patch configurations were considered to investigate the impact of patch diameter, interpatch distance and patch shape (Figure S7). Some additional experiments were made to cover the whole range of intertidal flow velocities (0.1 and 0.2 m/s). For each experiment, measurements were taken to record cross-flow velocity profiles around the vegetation patches (Figure S7). For more information about the experimental setup, the resulting data, and their availability, we refer to Vandenbruwaene et al. (2011) and Bouma et al. (2013). The characteristics of the different configurations used here are summarized in Table S1.

In this study, we use this data set to calibrate FRM and more particularly its bulk drag coefficient C_d. This is achieved by running a total of 78 simulations on the flume experiment domain (Figure 7a) reproducing each of the nine original vegetation patch configurations (Figure S7) sometimes with different incoming flow velocities (Table S1) and using different values of C_d (1, 2, 3, 5, 7, 10). The computational time for a simulation of a 30-min period is on average 4 min 39 s using five nodes of supercomputer, each with two 14-core Intel Xeon Processors E5-2680 v4 (i.e., 140 cores in total).

We use a normalized Taylor diagram (see explanations in section 2.4.1) to evaluate the accuracy of the different model results with respect to the flume measurements and consequently determine that the optimal C_d value is 5 (Figure 8). This is confirmed by statistics averaged over simulations of equal C_d (Table S2). With $C_d = 5$, FRM simulates flow velocities around vegetation patches with a mean error lower than 10% of the incoming flow velocity and a mean spatial correlation higher than 0.98 (Table S2). The good performance of FRM against flume measurements is illustrated in Figure 9 for a case with two square patches of 4 m^2. In general, those results give much confidence in the ability of FRM to simulate flow interactions with more complex vegetation configurations, for which flume measurements are not available to compare with.

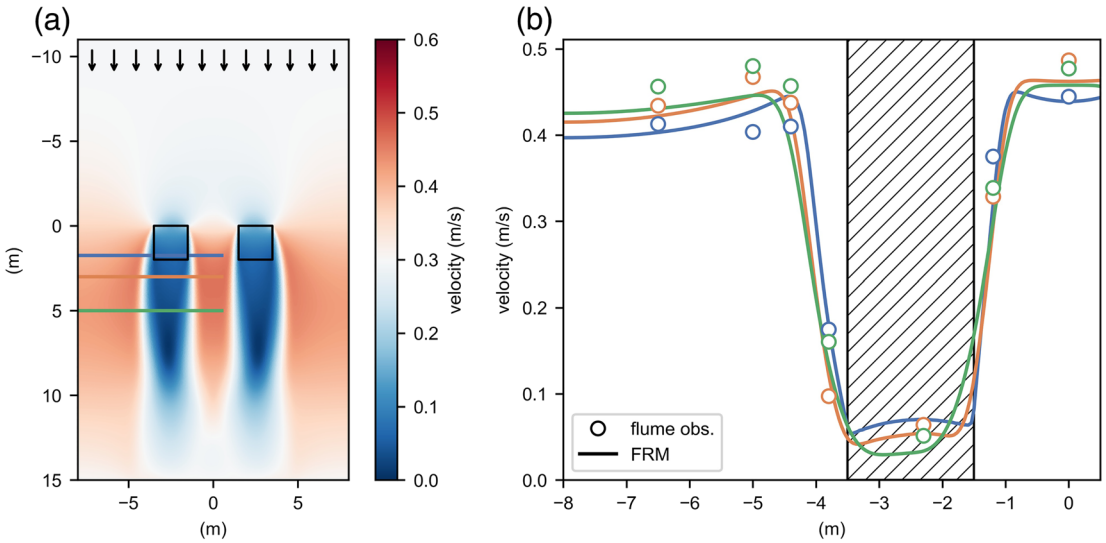

Figure 9. Magnitude of the flow velocities around vegetation patches simulated by FRM with $C_d = 5$ (flume experiment with two square patches of 4 m^2, an interpatch distance of 2 m, and an incoming flow velocity of 0.3 m/s). (a) Orthogonal view of the FRM simulation results. The black lines represent the vegetation patch contours. The arrows indicate the incoming flow direction. The color lines indicate the cross-flow profile locations. (b) Cross-flow profiles of the flow velocity measured in situ (color circles) and simulated with FRM (color lines). The hatched zone represents the area within (blue profile) or behind the vegetation patch (orange and green profiles).

2.5.2. Generation of the Convolution Mask

The convolution mask represents the flow perturbation around an elementary 25-by-25-cm vegetation patch located in the center of a 25-cm-resolution structured rectangular grid (section 2.2). Hence, the grid of the convolution mask must contain an odd number of cells in both along- and across-flow directions. The size of the convolution mask is chosen accordingly, with the domain width and the length in the wake of the vegetation patch slightly longer than in the original flume experiments (Figure 7b).

To generate the convolution mask, we run FRM on the convolution mask domain (Figure 7b) with an incoming flow velocity of 0.3 m/s and an initial water depth of 0.3 m. We then project the resulting fine-resolution flow velocity magnitudes on the 25-cm-resolution structured grid by averaging them over each rectangular grid cell. We finally divide the projected flow field by the incoming velocity to obtain the normalized convolution mask (Figure 4a). The computational time for a simulation of a 30-min period is 5 min 26 s using five nodes of a supercomputer, each with two 14-core Intel Xeon Processors E5-2680 v4 (i.e., 140 cores in total).

2.5.3. Randomly Distributed Vegetation Patches

The core of this study is the analysis of the flow interactions with randomly generated vegetation patch configurations at different stages of their lateral growth over a 32-m-wide, 50-m-long model domain (i.e., twice as wide and about twice as long as the original flume experiments). The computational domain is extended 4 m upstream and 8 m downstream to attenuate undesired boundary effects (Figure 7c). The different configurations considered are characterized by the number of patches N_p (1, 4, 16 or 64) and the mean patch surface area $\bar{S}_p$ (1/4, 1, 4 or 16 m^2).

The vegetation patches are generated in different steps. First, we initiate configurations with different numbers of patches (i.e., $N_p = 1$, 4, 16, or 64) by randomly selecting N_p vegetation grid cells (i.e., the patch centers). Then, we generate configurations with different mean patch surface areas (i.e., $\bar{S}_p = 1/4$, 1, 4 or 16 m^2) by expanding the patch centers. More specifically, in an iterative process, each vegetated grid cell is given a 50% chance to expand into its four neighbors, until the lowest mean patch surface area is reached (i.e., $\bar{S}_p = 1/4\,m^2$; Figure 2a). The iterative process is then repeated again until the next mean patch surface area is reached (i.e., $\bar{S}_p = 1\,m^2$; Figure 2b) and so on. Finally, each combination of N_p and $\bar{S}_p$ is replicated 10 times to account for stochasticity associated with the generation of specific random distributions. This leads to a total of 160 different vegetation patch configurations. However, with a total coverage higher than 50% of the model domain, the configurations with 16 patches of 16 m^2 do not represent patchy configurations anymore and are therefore disregarded. This leaves us with 150 configurations of randomly distributed vegetation patches.

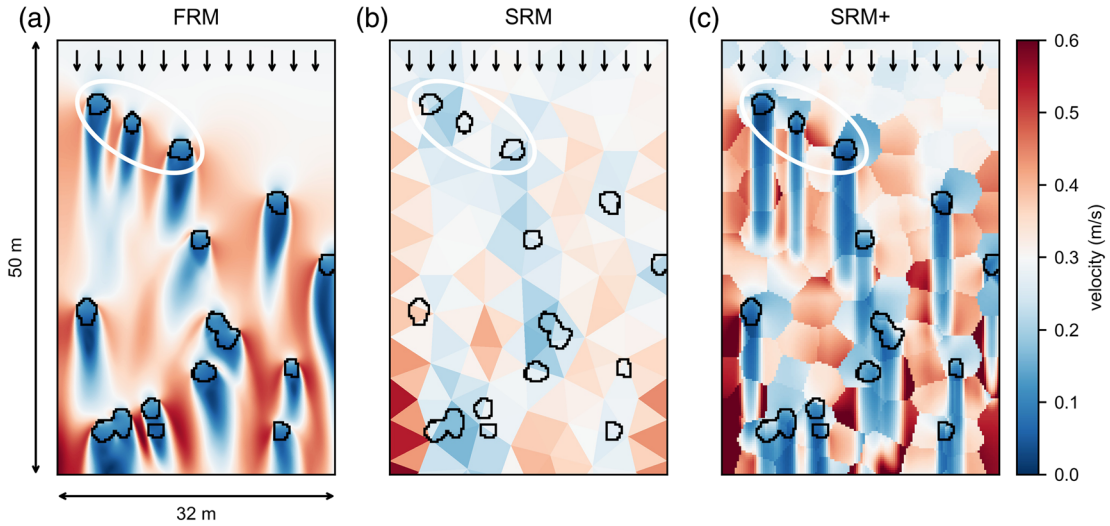

Figure 10. Magnitude of the flow velocities around vegetation patches (random configuration of 16 patches with a mean patch surface area of 4 m^2) simulated by FRM (a), SRM (b), and SRM+ (c). The black lines represent the contour of the vegetation patches. The white ellipses mark flow acceleration/deceleration patterns simulated by FRM and SRM+ but that SRM fails to reproduce. The single-headed arrows indicate the incoming flow direction. The double-headed arrows indicate the domain dimensions.

We use the three models (SRM, SRM+, and FRM) to simulate the flow through these 150 random patch configurations, with an incoming flow velocity of 0.3 m/s and an initial water depth of 0.3 m. Using 10 nodes of a supercomputer, each with two 14-core Intel Xeon Processors E5-2680 v4 (i.e., 280 cores in total), the computational time for a simulation of a 30-min period with FRM is on average 13 min 26 s. Using a single core of a 15-inch 2016 MacBook Pro with 2.6 GHz Intel Core i7, the same simulation takes between 1 and 2 s with SRM and an additional 0.16 s on average for the spatial refinement in SRM+.

The performance of the convolution method is then evaluated by comparing simulation results from SRM, SRM+, and FRM in normalized Taylor diagrams and using biogeomorphic metrics. In order to build comparable data sets, we interpolate linearly the SRM flow velocities on the structured vegetation grid, and we project the FRM flow velocities by averaging over each vegetation grid cell.

3. Results

The fine grid resolution of FRM allows for a detailed representation of the flow patterns around vegetation patches (Figure 10a). For example, we can clearly see the flow attenuation within and behind the patches, as well as the acceleration between and around them. We can also observe complex multidirectional patterns due to the asymmetric patch distribution. FRM is, however, computationally very expensive and not sustainable for applications on much larger domains of several km^2, which is ultimately the aim of our model development.

Because of its coarser grid resolution, SRM underestimates the intensity of the flow acceleration/deceleration patterns around small vegetation patches (Figure 10b). This is particularly clear in the three-patch zone marked in the upper left corner of the domain. While FRM predicts strong flow deceleration in the patch wakes (flow velocity lower than 0.1 m/s) and strong flow acceleration between the patches (flow velocity higher than 0.4 m/s), SRM seems to consider the three-patch zone as a single big low-density patch, with the surrounding flow only mildly impacted. With a 5-m grid resolution, SRM is nevertheless representative of today's state-of-the-art two-dimensional biogeomorphic models of tidal marshes (e.g., Belliard et al., 2015; Best et al., 2018; Bij de Vaate et al., 2020; Brckner et al., 2019; Mariotti, 2018; Sandi et al., 2018; Schwarz et al., 2014; Zhang et al., 2019).

The convolution method at the core of SRM+ is designed as a computationally efficient strategy to offset that behavior (Figure 10c). We can indeed observe that SRM+ is able to represent the flow deceleration/acceleration patterns around vegetation patches much better than SRM. This is particularly obvious in the three-patch zone marked in the upper left corner of the domain. SRM+ seems able to mimic, although not perfectly, the flow deceleration behind patches and the flow acceleration between patches as observed

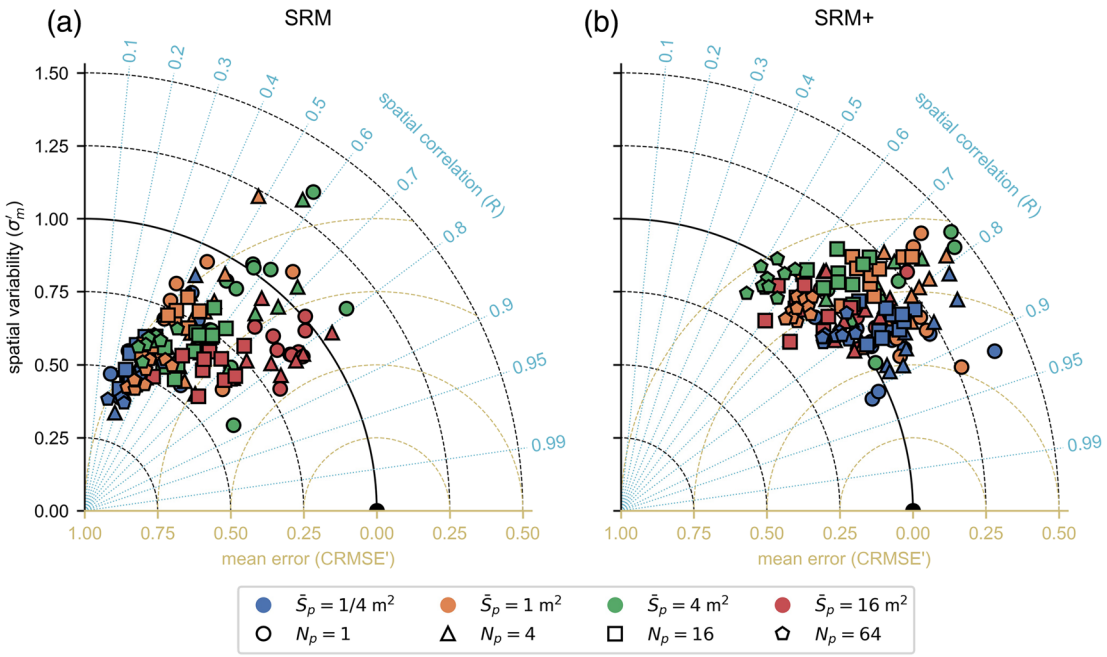

Figure 11. Normalized Taylor diagrams (see explanations in section 2.4.1) comparing the performance of 150 SRM (a) and SRM+ (b) simulations for different randomly distributed vegetation patch configurations. The statistics are obtained by comparison with the reference FRM simulation results. The marker shapes and colors indicate, respectively, the number of patches N_p and their mean surface area $\bar{S}_p$. Multiple markers with the same shape and color correspond to random replicates of the same combination of N_p and $\bar{S}_p$.

in the reference simulation (Figure 10a), whereas SRM completely fails to reproduce these flow patterns (Figure 10b). Yet, the convolution method is computationally very efficient. For the simulations presented herein, the four-step methodology for spatial refinement takes about 10% extra computational time, as compared to a regular SRM simulation. What the convolution method fails to address though is to recreate secondary flows where SRM is not able to simulate them itself. Here we reach the limit of what our approach can achieve.

Using a normalized Taylor diagram (Figure 11a) and statistics averaged over simulations of equal $\bar{S}_p$ (Table S3), we can show that in general the accuracy of SRM increases with the patch size (CRMSE′ $\rightarrow$ 0, $\sigma'_m \rightarrow 1$ and $R \rightarrow 1$). This is the expected behavior as the 5-m grid resolution of SRM becomes more and more suitable for representing the overall shape of the patches when their size increases. However, our results suggest that SRM overall fails to represent the flow deceleration/acceleration patterns around vegetation patches, in terms of both intensity ($\sigma'_m \ll 1$) and spatial correlation ($R \ll 1$). This is especially the case for smaller patches ($\bar{S}_p \ll 5$ m).

It is more difficult to detect a clear trend for SRM+ based on the patch size, although we can observe that it performs better for the smallest patches (Figure 11b). This is confirmed by the averaged statistics in Table S3 (lowest CRMSE′, second closest σ'_m to 1 and highest R). This is because smaller patches are more similar to the elementary patch of the convolution mask (a patch of 1/4 m² corresponds to a combination of four elementary patches). The main assumption supporting the convolution method is that the flow velocity field around complex vegetation patterns can be approximated by combining the impact that single elementary vegetation units would have separately on the flow (section 2.2.1). Our results indicate that this assumption especially holds for smaller patches but that its validity decreases with the patch size. However, we can also observe that SRM+ performs slightly better for the largest patches than for those of intermediate sizes (second lowest CRMSE′, closest σ'_m to 1 and third highest R). This is because the performance of SRM at the scale of those patches is already very close to what SRM+ can achieve.

When comparing the two diagrams in Figure 11, we can notice some trends indicating an improvement in model accuracy from SRM to SRM+. The most striking pattern is the improvement in spatial variability (i.e., a better representation of the intensity of flow acceleration/deceleration patterns) with values of σ'_m increasing closer to 1. The clear underestimation of the intensity of the flow perturbation patterns with SRM

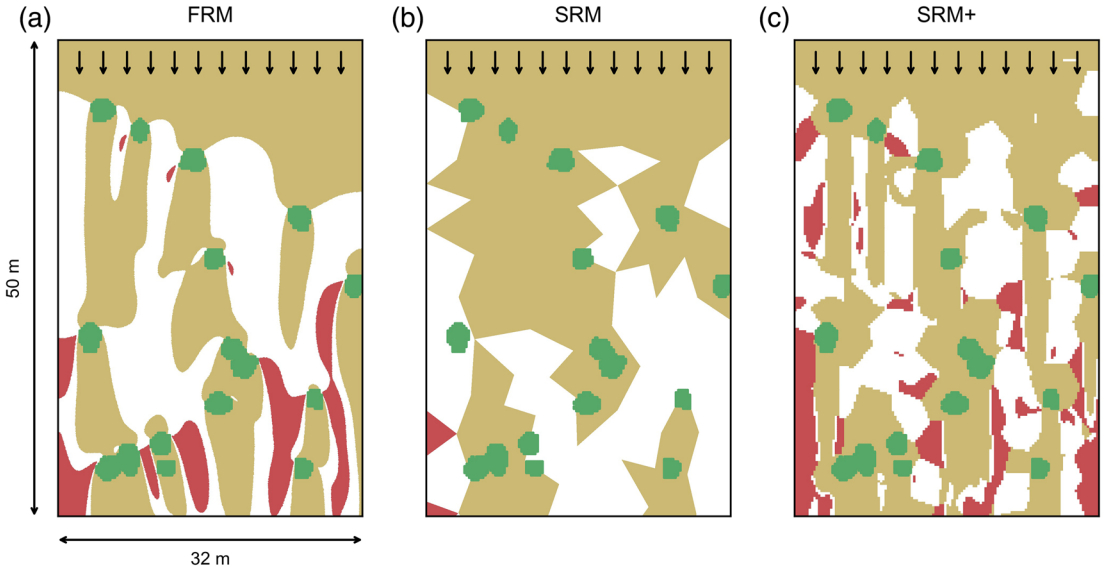

Figure 12. Zones of potential plant growth (in yellowish, where $\|\tau_b\| < \tau_v$) and potential channel incision (in red, where $\|\tau_b\| > \tau_e$) resulting from flow velocities around vegetation patches (in green) simulated by FRM (a), SRM (b), and SRM+ (c) for a random configuration of 16 patches with a mean patch surface area of 4 m^2. The single-headed arrows indicate the incoming flow direction. The double-headed arrows indicate the domain dimensions.

($\sigma'_m \ll 1$) becomes a mild overestimation with SRM+ ($\sigma'_m > 1$). The spatial correlation of the flow perturbation patterns also improves, with most values of R ranging between 0.2 and 0.8 with SRM and between 0.5 and 0.9 with SRM+. Finally, we can also observe a decrease in the mean error, although limited to the smallest patches. On average, the mean error, spatial variability, and spatial correlation improve by, respectively, 13%, 66%, and 49% from SRM to SRM+.

In general, the real power of the convolution method is that it does not deteriorate SRM results in areas where it performs best, while simultaneously improving the flow field accuracy where it is appropriate, that is, within and around vegetation patches that are substantially smaller than the SRM grid size. Indeed, if the trends described in the previous paragraph are not so clear for the largest patches, they become stronger and stronger for decreasing patch sizes (Figure 11 and Table S3) as the validity of the main assumption supporting the convolution method increases.

The improved performance from SRM to SRM+ has important consequences for the modeling of biogeomorphic feedbacks. For example, we can observe from FRM simulation results that potential plant growth is limited to the wakes of the patches and that channel incision can occur between them (Figure 12a). Because SRM underestimates the intensity of the flow acceleration/deceleration patterns around small vegetation patches, it also overestimates the extent of the zone for potential plant growth and almost completely fails to reproduce the favorable conditions for channel incision (Figure 12b). SRM+ on the contrary seems able to recreate at least partially the spatial patterns for potential plant growth and channel incision observed with FRM (Figure 12c).

In general, our results show evidence that biogeomorphic scale-dependent feedbacks can be simulated more accurately with the convolution method (Figure 13). Indeed, for the 150 configurations of randomly distributed vegetation patches considered here, the relative error in total net sedimentation rate with SRM+ is either very low ($\bar{S}_p \leq 1\,m^2$) or significantly smaller than with SRM ($\bar{S}_p \geq 4\,m^2$—Figure 13a). Similarly, the relative error in habitable surface area with SRM+ is either significantly smaller than with SRM ($\bar{S}_p \leq 4\,m^2$) or of the same order of magnitude ($\bar{S}_p = 16\,m^2$). The difference between the two modeling approaches decreases with the patch size (Figure 13b). On average, the errors in net sedimentation rate and habitable surface area improve by, respectively, 66% and 39% from SRM to SRM+. A substantial part of the residual error after application of the convolution method is most probably due to its inability to recreate secondary flows that SRM is not able to simulate itself.

Another interesting observation is that the relative error in total net sedimentation rate increases with the patch size for both modeling approaches (Figure 13a). This is, however, not contradictory with our previous

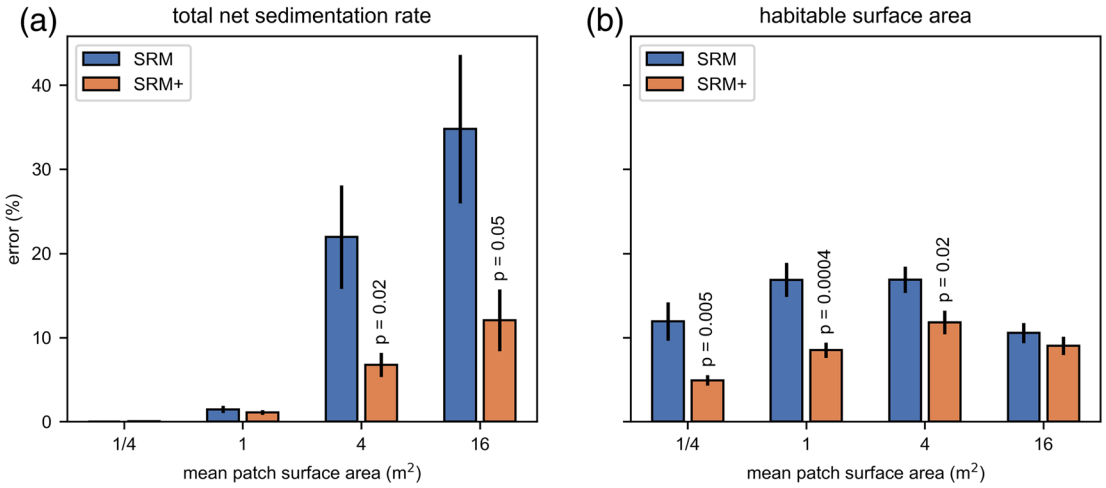

Figure 13. Relative error in total net sedimentation rate (a) and in habitable surface area (b) averaged over simulations of equal mean patch surface area $\bar{S}_p$. The simulations are performed using SRM (blue) and SRM+ (orange). The errors are obtained in comparison with the reference FRM simulation results. The black lines represent the corresponding standard errors. The p values are the results of statistical tests (T test) to determine if the relative errors for a given $\bar{S}_p$ value are significantly different whether SRM or SRM+ is used (only shown for $p \leq 0.05$).

observation that SRM accuracy increases with the patch size (Figure 11a). Indeed, for patches smaller than or equal to 1 m^2, the flow acceleration around them is too low to trigger much erosion, so that $E \simeq 0$ and $F_{sed} \simeq w_s C_S$ in all cases and with all three modeling approaches. Hence, the relative error is very low. In contrast, the flow acceleration is much more important around patches larger than or equal to 4 m^2, which leads to more erosion around and between vegetation patches and hence lower, possibly negative, total net sedimentation rate. The absolute error $|F_{sed} - F_{sed}^{FRM}|$ probably decreases with the patch size, due to increase of SRM accuracy. However, the decrease of $|F_{sed}^{SRM}|$ in the denominator of Equation 23 is more intense. Hence, the relative error in total net sedimentation rate increases with the patch size.

Finally, the relative error in habitable surface area for SRM increases with the patch size for patches smaller than or equal to 1 m^2 and decreases for patches larger than or equal to 4 m^2 (Figure 13b). This is the result of two contrasting trends. On the one hand, the absolute error $|S_{hab} - S_{hab}^{FRM}|$ in the numerator of Equation 24 probably decreases with the patch size due to increase of SRM accuracy. On the other hand, the habitable surface area obtained with FRM in the denominator of Equation 24 also decreases with the patch size, due to a larger zone of strong flow acceleration. For smaller patches, the second trend is more important, so the relative error increases. For larger patches on the contrary, the first trend is dominant, so the relative error decreases. For SRM+, the general trend is easier to read. The relative error is smallest for the smallest patches because the convolution method is more efficient at that scale.

4. Discussion

Biogeomorphology is a relatively new field of research that studies interactions between organisms and the development of landforms, with recently several major advances in coastal and fluvial systems (e.g., Caponi & Siviglia, 2018; Kearney & Fagherazzi, 2016; Kirwan et al., 2016; Kleinhans et al., 2015; Lauzon & Murray, 2018; Piliouras & Kim, 2019; Schwarz et al., 2018). There is field evidence that, for some vegetation species, early stage of colonization can occur in heterogeneous patterns of small-scale vegetation patches (order of m^2 Balke et al., 2012; Bouma et al., 2007; Nepf, 2012; Van der Wal et al., 2008; van de Vijsel et al., 2020) which are known to have important impacts on the biogeomorphic developments at the landscape scale (order of km^2 Folkard, 2019; Larsen, 2019). Prominent examples are the formation of channel networks by differential erosion and deposition patterns (Schwarz et al., 2018; Taramelli et al., 2018; Temmerman et al., 2007) and the heterogeneous development of larger vegetated landforms (Chen et al., 2012; Follett & Nepf, 2012; Gurnell, 2014). Yet, because vegetation patchiness often occurs at their subgrid scale, current biogeomorphic models are not able to include these small-scale interactions in the processes they solve (Le Hir et al., 2007). Here we present a novel computationally efficient methodology that fills this technological gap. Our new method allows biogeomorphic models to account for interactions with fine-scale vegetation

structures by redistributing flow velocities at the subgrid scale using a convolution algorithm. As such, it paves the way for explicit simulations of the scale-dependent feedbacks around pioneer patches of vegetation (order of m^2) together with their long-term impact (order of decades) at the landscape scale (order of km^2).

The main assumption behind our convolution method is that the flow velocities around complex vegetation patterns can be approximated by combining the impact that single elementary vegetation units would have separately on the flow (section 2.2.1). Our results indicate that this assumption especially holds for smaller subgrid patches but that its validity decreases with the patch size (Figure 11b). At the same time, our results reveal that the convolution method does not deteriorate the quality of the flow velocities around bigger patches that are already well simulated at coarse resolution. That filter-like behavior is the real power of our novel approach.

If the convolution method allows to mimic relatively well the flow deceleration behind patches and the flow acceleration between patches, it fails at representing the secondary flows that standard-resolution models also miss (Figure 10). This is a limitation of the method that is intrinsic to its design. Indeed, combining impacts of single vegetation grid cells proved to perform quite well for cumulative effects within a single patch. However, nothing is envisaged in the method to account for asymmetric interactions between distanced grid cells or patches. That does not mean that our convolution method completely fails at representing secondary flows. Here used as spatial refinement for standard-resolution biogeomorphic models (section 2.2.2) it simply fails at recreating secondary flows at the subgrid scale. Besides, it is worth mentioning that secondary flows occurring in our test cases are in reality linked to three-dimensional hydrodynamics and turbulence (Nepf, 2012; Ortiz et al., 2013), which falls beyond the scope of the present scaling approach. Still, it means that some emergent hydrodynamic phenomena resulting from the presence of patchy vegetation are not included in our modeling approach, and hence the latter produces a world more simple than it actually is. This can have consequences in terms of emergent properties at larger scales, such as complexity of creek networks, sedimentation processes, or vegetation patterns.

We purposely restrict our study to steady state conditions to keep the focus on our novel methodology and its efficiency to spatially refine flow velocities from standard-resolution models. The transposition to fluctuating flow regimes is, however, rather straightforward (see, e.g., supporting information Text S3 and Figure S6). Applying the convolution method at every time step of a standard-resolution model is probably not the most optimal strategy. For example, this would lead to an increase in computational time by a factor of the order of 10^3 for the random-patch test cases of this study (section 2.5.3). This is still significantly smaller than a process-based model at the scale of the vegetation grid (estimated factor of the order of 10^4) but probably not worth the gain in accuracy. Yet, applying the convolution method at specific time steps would allow to significantly improve the quantification of important biogeomorphic processes at relatively low additional computational cost (e.g., only an estimated factor of about 2 when applied every 15 min over a semidiurnal tidal cycle in a salt marsh environment).

Important aspects of the scale-dependent biogeomorphic feedbacks are the increase of sediment deposition within and behind vegetation patches and the potential erosion around and between them (Bouma et al., 2007; de Lima et al., 2015; Gu et al., 2018; Licci et al., 2019; Meire et al., 2014; Ortiz et al., 2013; Schwarz et al., 2015; Zong & Nepf, 2010). However, when vegetation patches or interpatch distances are too small, that is, if they are of the same order of magnitude or smaller than the grid size, biogeomorphic models are not able to accurately quantify these sediment fluxes (e.g., Figure 12b). In this paper, we showed that the convolution can be used to refine the estimation of these subgrid-scale erosion and deposition processes (Figures 12c and 13a).

Other important aspects of the scale-dependent biogeomorphic feedbacks are the improved conditions for plant growth within and behind vegetation patches, due to flow deceleration and increase of nutrient-rich sediment deposition (positive feedbacks Kondziolka & Nepf, 2014; Schoelynck et al., 2012; Yamasaki et al., 2019) and the deteriorated plant growth conditions around and between patches, due to flow acceleration and sediment erosion that may dislodge seedlings and uproot plants (negative feedbacks Bouma et al., 2007; Temmerman et al., 2007; van Wesenbeeck et al., 2008). Fine-scale vegetation dynamic models require spatially detailed hydrogeomorphic information to determine accurately where vegetation is likely to grow. In this paper, we demonstrated that the convolution method can be used to that end (Figures 12c and 13b).

Multiscale coupling between a relatively coarse-resolution process-based hydrogeomorphic model (e.g., similar to SRM) and a much finer-resolution reduced-complexity cellular automaton to describe the complex interactions between vegetation and its environment (e.g., on a grid similar to the vegetation grid) is certainly one way to go for present and future research in biogeomorphology (Fonstad, 2006; Solari et al., 2016). In that framework, the convolution method presented in this paper can be used for the one-way coupling from the relatively coarse-scale hydrogeomorphic model to the fine-scale vegetation cellular automaton. Indeed, we showed that the convolution method allows for better determination of the areas where vegetation is likely to settle, grow, and survive, as compared with simply using the coarse-resolution velocity flow fields (Figures 12 and 13b). In the same framework, our results suggest that the convolution method could also be used to simulate water-bed exchange processes at fine resolution (Figures 12 and 13a). This would lead to more accurate information of the spatial patterns of erosion and deposition and hence better representation of their impact on the vegetation dynamics. The refined estimation of the net sedimentation rates would also benefit the coarse-resolution hydrogeomorphic model, which would transport more accurate quantities of suspended sediments. Finally, this would imply to deal with subgrid-scale topographic heterogeneity, which has already been addressed successfully in recent studies (Volp et al., 2013; Wu et al., 2016).

Other aspects of the multiscale coupling, however, cannot be addressed by the convolution method. For example, the spatial patterns of vegetation distribution at the subgrid scale are in general not considered when calculating the vegetation resistance on the flow. Instead, only the mean subgrid biomass is accounted for, like we do in Equation 19. Yet, recent studies have shown that subgrid-scale vegetation patchiness can have far-reaching hydrogeomorphic implications at the landscape scale (Larsen et al., 2017; Wright et al., 2018). This must be addressed to achieve two-way multiscale biogeomorphic coupling.

Recently, major advances in the field of applied biogeomorphology concerned the exploration of nature-based solutions for coastal management (Huguet et al., 2018; Morris et al., 2018; Narayan et al., 2016; Temmerman & Kirwan, 2015; Thorslund et al., 2017; Van Coppenolle & Temmerman, 2020; van Wesenbeeck et al., 2014; Vuik et al., 2016). It builds on the premise that we can improve coastal safety and flood protection by restoring natural ecosystems along the coastal zone. It presumes, however, that establishment of vegetation is guaranteed once space is made available, which is not always the case. To improve coastal safety and design solutions that really work, we need models that are able to assess whether vegetation establishment will actually take place but also to predict what will be their ecological and geomorphological impact on the long term and at the landscape scale. Therefore, techniques like our subgrid method that integrate small-scale biogeomorphic feedback processes into large-scale models are crucial tools to design successful nature-based solutions and hence a safer future. The convolution method presented in this paper is a crucial part of the novel multiscale biogeomorphic model Demeter, which we are currently developing to achieve that goal.

5. Conclusion

In this paper, we described a novel methodology to account for subgrid-scale interactions between water flow and patchy vegetation in a relatively coarse-scale hydrodynamic model. Our new method is very computationally efficient, as it combines coarse-scale flow velocities with the convolution product between fine-scale patchy vegetation distribution and the flow perturbation due to one single vegetated grid cell. With simple test cases, we showed that applying the convolution method substantially improved flow velocity results of a coarse-resolution hydrodynamic model (mean error, spatial variability, and spatial correlation, respectively, 13%, 66%, and 49% better on average). If flow perturbations around each vegetation grid cell are not simulated with the same level of accuracy as with more expensive finer-resolution models, we estimate that our multiscale approach could reduce the computational time of real-life fluctuating flow simulations by several orders of magnitude.

Our new methodology acts like a filter on the coarse-scale flow velocities. We have indeed shown evidence that, on the one hand, the convolution method improves significantly the flow velocity patterns where it is necessary (i.e., around smaller vegetation patches) and, on the other hand, does not deteriorate the flow velocity patterns where they are already well described (i.e., around larger patches). Using simple examples, we have also shown the potential of the method for better estimation of the subgrid-scale erosion and deposition rates, as well as for more detailed determination of the areas where vegetation is likely to expand around vegetation patches.

Hence, we demonstrated that our convolution method is one part of a solution toward more computationally efficient multiscale biogeomorphic modeling, which may allow to study the impact of scale-dependent feedbacks around patchy vegetation distributions (order of m^2) over larger ecosystems (order of km^2) than what was possible to date.

Appendix A: Normalized Taylor Diagrams

Let m_i and o_i $(i = 1, \ldots, N)$ be modeled and observed data sets of any scalar variable, where N is the number of data. Their respective mean and standard deviation are defined as

$$\bar{m} = \frac{1}{N}\sum_{i=1}^{N} m_i, \tag{A1}$$

$$\bar{o} = \frac{1}{N}\sum_{i=1}^{N} o_i, \tag{A2}$$

$$\sigma_m^2 = \frac{1}{N}\sum_{i=1}^{N} (m_i - \bar{m})^2, \tag{A3}$$

$$\sigma_o^2 = \frac{1}{N}\sum_{i=1}^{N} (o_i - \bar{o})^2. \tag{A4}$$

The bias (BIAS), the center root mean square error (CRMSE), and the correlation coefficient (R) are given by

$$\mathrm{BIAS} = \bar{m} - \bar{o}, \tag{A5}$$

$$\mathrm{CRMSE}^2 = \frac{1}{N}\sum_{i=1}^{N} \left((m_i - \bar{m}) - (o_i - \bar{o})\right)^2, \tag{A6}$$

$$R = \frac{1}{\sigma_m \sigma_o}\frac{1}{N}\sum_{i=1}^{N} (m_i - \bar{m})(o_i - \bar{o}). \tag{A7}$$

The CRMSE is related to σ_m, σ_o and R as follows:

$$\mathrm{CRMSE}^2 = \sigma_m^2 + \sigma_o^2 - 2\sigma_m \sigma_o R. \tag{A8}$$

Making use of the law of cosines, Equation A8 can be visualized in a polar coordinate plot (i.e., the Taylor diagram) where the radial coordinate is the standard deviation and the angular coordinate is $\arccos(R)$. The CRMSE then appears as the distance from the position of the observed data set $(\sigma_o, 0)$.

Equation A8 has the dimension of the principal variable squared. Dividing all terms by σ_o^2 leads to dimensionless quantities and the normalized Taylor diagram in which the position of the observed data set is $(1, 0)$:

$$\mathrm{CRMSE}'^2 = \sigma_m'^2 + 1 - 2\sigma_m' R, \tag{A9}$$

with

$$\mathrm{CRMSE}' = \frac{1}{\sigma_o}\mathrm{CRMSE}, \tag{A10}$$

$$\sigma_m' = \frac{\sigma_m}{\sigma_o}. \tag{A11}$$

With classical Taylor diagrams, the performance of one or several model runs is compared against one single observed data set. Indeed, different observed data sets have different standard deviations, σ_o, and hence different positions $(\sigma_o, 0)$ in the diagram. A separate diagram is therefore required for each observed data set. With normalized Taylor diagrams, the position of the observed data set is always $(1, 0)$. Therefore, different observed data sets, possibly from different variables, can be displayed on a single diagram.

Data Availability Statement

All software programs and supporting data set to reproduce the figures and tables of this paper are available on the general-purpose open-access repository Zenodo. This includes the Python module *VFC* where the convolution method is implemented (Gourgue et al., 2020a), the Python module *NTaylor* to create normalized Taylor diagrams (Gourgue, 2020a), the multipurpose Python toolbox *OGTools* (Gourgue, 2020b), and the supporting data set (Gourgue et al., 2020b).

Acknowledgments
This project has received funding from the VNSC (Vlaams-Nederlandse Scheldecommissie) and the European Union's Horizon 2020 research and innovation program under the Marie Skłodowska-Curie grant agreement 798222. The computational resources and services used in this work were provided by the VSC (Flemish Supercomputer Center) funded by the Research Foundation—Flanders (FWO) and the Flemish Government—department EWI. The flume experiments have been supported by the EU 6th Framework Program, Integrated Infrastructure Initiative HYDRALAB III within the Transnational Access Activities, contract 022441. We are thankful to Angela Gurnell and Jonas Schoelynck for sharing photographs (Figure 1) and Dante Horemans for his critical review of the convolution method (section 2.2).

References

Adams, M. P., Hovey, R. K., Hipsey, M. R., Bruce, L. C., Ghisalberti, M., Lowe, R. J., et al. (2016). Feedback between sediment and light for seagrass: Where is it important? *Limnology and Oceanography*, *61*, 1937–1955. https://doi.org/10.1002/lno.10319

Balke, T., Klaassen, P. C., Garbutt, A., van der Wal, D., Herman, P. M. J., & Bouma, T. J. (2012). Conditional outcome of ecosystem engineering: A case study on tussocks of the salt marsh pioneer Spartina anglica. *Geomorphology*, *153–154*, 232–238. https://doi.org/10.1016/j.geomorph.2012.03.002

Baptist, M. J., Babovic, V., Rodríguez Uthurburu, J., Keijzer, M., Uittenbogaard, R. E., Mynett, A., & Verwey, A. (2007). On inducing equations for vegetation resistance. *Journal of Hydraulic Research*, *45*, 435–450. https://doi.org/10.1080/00221686.2007.9521778

Belliard, J.-P., Toffolon, M., Carniello, L., & D'Alpaos, A. (2015). An ecogeomorphic model of tidal channel initiation and elaboration in progressive marsh accretional contexts. *Journal of Geophysical Research: Earth Surface*, *120*, 1040–1064. https://doi.org/10.1002/2015JF003445

Bernhardt, C. E., & Willard, D. A. (2009). Response of the Everglades ridge and slough landscape to climate variability and 20th century water management. *Ecological Applications*, *19*, 1723–1738. https://doi.org/10.1890/08-0779.1

Best, U. S. N., Van der Wegen, M., Dijkstra, J., Willemsen, P. W. J. M., Borsje, B. W., & Roelvink, D. J. A. (2018). Do salt marshes survive sea level rise? Modelling wave action, morphodynamics and vegetation dynamics. *Environmental Modelling and Software*, *109*, 152–166. https://doi.org/10.1016/j.envsoft.2018.08.004

Bij de Vaate, I., Brckner, M. Z. M., Kleinhans, M. G., & Schwarz, C. (2020). On the impact of salt marsh pioneer species assemblages on the emergence of intertidal channel networks. *Water Resources Research*, *56*, e2019WR025942. https://doi.org/10.1029/2019WR025942

Bouma, T. J., Friedrichs, M., Wesenbeeck, B. K. V., Temmerman, S., Graf, G., & Herman, P. M. J. (2009). Density-dependent linkage of scale-dependent feedbacks: A flume study on the intertidal macrophyte Spartina anglica. *Oikos*, *118*, 260–268. https://doi.org/10.1111/j.1600-0706.2008.16892.x

Bouma, T. J., Temmerman, S., van Duren, L. A., Martini, E., Vandenbruwaene, W., Callaghan, D. P., et al. (2013). Organism traits determine the strength of scale-dependent bio-geomorphic feedbacks: A flume study on three intertidal plant species. *Geomorphology*, *180–181*, 57–65. https://doi.org/10.1016/j.geomorph.2012.09.005

Bouma, T. J., van Duren, L. A., Temmerman, S., Claverie, T., Blanco-Garcia, A., Ysebaert, T., & Herman, P. M. J. (2007). Spatial flow and sedimentation patterns within patches of epibenthic structures: Combining field, flume and modelling experiments. *Continental Shelf Research*, *27*, 1020–1045. https://doi.org/10.1016/j.csr.2005.12.019

Brckner, M. Z. M., Schwarz, C., Dijk, W. M., Oorschot, M., Douma, H., & Kleinhans, M. G. (2019). Salt marsh establishment and eco engineering effects in dynamic estuaries determined by species growth and mortality. *Journal of Geophysical Research: Earth Surface*, *124*, 2962–2986. https://doi.org/10.1029/2019JF005092

Bryan, K. R., Nardin, W., Mullarney, J. C., & Fagherazzi, S. (2017). The role of cross-shore tidal dynamics in controlling intertidal sediment exchange in mangroves in C Lao Dung, Vietnam. *Continental Shelf Research*, *147*, 128–143. https://doi.org/10.1016/j.csr.2017.06.014

Caponi, F., & Siviglia, A. (2018). Numerical modeling of plant root controls on gravel bed river morphodynamics. *Geophysical Research Letters*, *45*, 9013–9023. https://doi.org/10.1029/2018GL078696

Carr, J. A., D'Odorico, P., McGlathery, K. J., & Wiberg, P. L. (2016). Spatially explicit feedbacks between seagrass meadow structure, sediment and light: Habitat suitability for seagrass growth. *Advances in Water Resources*, *93*, 315–325. https://doi.org/10.1016/j.advwatres.2015.09.001

Chen, Z., Ortiz, A., Zong, L., & Nepf, H. (2012). The wake structure behind a porous obstruction and its implications for deposition near a finite patch of emergent vegetation. *Water Resources Research*, *48*, W09517. https://doi.org/10.1029/2012WR012224

Corenblit, D., Baas, A., Balke, T., Bouma, T., Fromard, F., Garfanomez, V., et al. (2015). Engineer pioneer plants respond to and affect geomorphic constraints similarly along water terrestrial interfaces world wide. *Global Ecology and Biogeography*, *24*, 1363–1376. https://doi.org/10.1111/geb.12373

Cornacchia, L., van de Koppel, J., van der Wal, D., Wharton, G., Puijalon, S., & Bouma, T. J. (2018). Landscapes of facilitation: How self organized patchiness of aquatic macrophytes promotes diversity in streams. *Ecology*, *99*, 832–847. https://doi.org/10.1002/ecy.2177

Crosato, A., & Saleh, M. S. (2011). Numerical study on the effects of floodplain vegetation on river planform style. *Earth Surface Processes and Landforms*, *36*, 711–720. https://doi.org/10.1002/esp.2088

D'Alpaos, A., Da Lio, C., & Marani, M. (2012). Biogeomorphology of tidal landforms: Physical and biological processes shaping the tidal landscape. *Ecohydrology*, *5*, 550–562. https://doi.org/10.1002/eco.279

D'Alpaos, A., Lanzoni, S., Marani, M., Fagherazzi, S., & Rinaldo, A. (2005). Tidal network ontogeny: Channel initiation and early development. *Journal of Geophysical Research*, *110*, F2001. https://doi.org/10.1029/2004JF000182

D'Alpaos, A., Lanzoni, S., Marani, M., & Rinaldo, A. (2007). Landscape evolution in tidal embayments: Modeling the interplay of erosion, sedimentation, and vegetation dynamics. *Journal of Geophysical Research*, *112*, F01008. https://doi.org/10.1029/2010JF001788

de Lima, P. H. S., Janzen, J. G., & Nepf, H. M. (2015). Flow patterns around two neighboring patches of emergent vegetation and possible implications for deposition and vegetation growth. *Environmental Fluid Mechanics*, *15*, 881–898. https://doi.org/10.1007/s10652-015-9395-2

Einstein, H. A., & Krone, R. B. (1962). Experiments to determine modes of cohesive sediment transport in salt water. *Journal of Geophysical Research*, *67*, 1451–1461.

Folkard, A. M. (2019). Biophysical interactions in fragmented marine canopies: Fundamental processes, consequences, and upscaling. *Frontiers in Marine Science*, *6*, 279. https://doi.org/10.3389/fmars.2019.00279

Follett, E. M., & Nepf, H. M. (2012). Sediment patterns near a model patch of reedy emergent vegetation. *Geomorphology*, *179*, 141–151. https://doi.org/10.1016/j.geomorph.2012.08.006

Fonstad, M. A. (2006). Cellular automata as analysis and synthesis engines at the geomorphology ecology interface. *Geomorphology*, *77*, 217–234. https://doi.org/10.1016/j.geomorph.2006.01.006

Francis, R. A., Corenblit, D., & Edwards, P. J. (2009). Perspectives on biogeomorphology, ecosystem engineering and self-organisation in island-braided fluvial ecosystems. *Aquatic Sciences*, *71*, 290–304. https://doi.org/10.1007/s00027-009-9182-6

Geuzaine, C., & Remacle, J. F. (2009). Gmsh: A 3-D finite element mesh generator with built-in pre- and post-processing facilities. *International Journal for Numerical Methods in Engineering*, *79*, 1309–1331. https://doi.org/10.1002/nme.2579

Gourgue, O. (2020a). NTaylor: Normalized Taylor diagram Python module (Version 1.0). https://doi.org/10.5281/zenodo.3715535

Gourgue, O. (2020b). OGTools (Version 1.1). https://doi.org/10.5281/zenodo.3994952

Gourgue, O., van Belzen, J., Schwarz, C., Bouma, T. J., van de Koppel, J., & Temmerman, S. (2020a). VFC: Vegetation/Flow Convolution Python module (Version 1.0.1). https://doi.org/10.5281/zenodo.3994961

Gourgue, O., van Belzen, J., Schwarz, C., Bouma, T. J., van de Koppel, J., & Temmerman, S. (2020b). Supporting data for "A convolution method to assess subgrid-scale interactions between flow and patchy vegetation in biogeomorphic models" (Version 1.1). https://doi.org/10.5281/zenodo.3995321

Gu, J., Shan, Y., Liu, C., & Liu, X. (2018). Feedbacks of flow and bed morphology from a submerged dense vegetation patch without upstream sediment supply. *Environmental Fluid Mechanics*, *153*, 1–19. https://doi.org/10.1007/s10652-018-9633-5

Gurnell, A. (2014). Plants as river system engineers. *Earth Surface Processes and Landforms*, *39*, 4–25. https://doi.org/10.1002/esp.3397

Heffernan, J. B., Watts, D. L., & Cohen, M. J. (2013). Discharge competence and pattern formation in peatlands: A meta-ecosystem model of the Everglades ridge-slough landscape. *PLOS ONE*, *8*(5), e64174. https://doi.org/10.1371/journal.pone.0064174

Hervouet, J.-M. (2007). *Hydrodynamics of free surface flows: Modelling with the finite element method*. Hoboken, NJ, United States: Wiley-Blackwell. https://doi.org/10.1002/9780470319628

Huguet, J. R., Bertin, X., & Arnaud, G. (2018). Managed realignment to mitigate storm-induced flooding: A case study in La Faute-sur-mer, France. *Coastal Engineering*, *134*, 168–176. https://doi.org/10.1016/j.coastaleng.2017.08.010

Istanbulluoglu, E., & Bras, R. L. (2005). Vegetation modulated landscape evolution: Effects of vegetation on landscape processes, drainage density, and topography. *Journal of Geophysical Research*, *110*, F02012. https://doi.org/10.1029/2004JF000249

Kärnä, T., & Baptista, A. M. (2016). Evaluation of a long-term hindcast simulation for the Columbia River estuary. *Ocean Modelling*, *99*, 1–14. https://doi.org/10.1016/j.ocemod.2015.12.007

Kearney, W. S., & Fagherazzi, S. (2016). Salt marsh vegetation promotes efficient tidal channel networks. *Nature Communications*, *7*, 12,287. https://doi.org/10.1038/ncomms12287

Kirwan, M. L., Temmerman, S., Skeehan, E. E., Guntenspergen, G. R., & Fagherazzi, S. (2016). Overestimation of marsh vulnerability to sea level rise. *Nature Climate Change*, *6*, 253–260. https://doi.org/10.1038/nclimate2909

Kleinhans, M. G., Braudrick, C., van Dijk, W. M., van de Lageweg, W. I., Teske, R., & van Oorschot, M. (2015). Swiftness of biomorphodynamics in Lilliput- to giant-sized rivers and deltas. *Geomorphology*, *244*, 56–73. https://doi.org/10.1016/j.geomorph.2015.04.022

Kondziolka, J. M., & Nepf, H. M. (2014). Vegetation wakes and wake interaction shaping aquatic landscape evolution. *Limnology and Oceanography: Fluids and Environments*, *4*, 106–119. https://doi.org/10.1215/21573689-2846314

Larsen, L. G. (2019). Multiscale flow-vegetation-sediment feedbacks in low-gradient landscapes. *Geomorphology*, *334*, 165–193. https://doi.org/10.1016/j.geomorph.2019.03.009

Larsen, L. G., & Harvey, J. W. (2011). Modeling of hydroecological feedbacks predicts distinct classes of landscape pattern, process, and restoration potential in shallow aquatic ecosystems. *Geomorphology*, *126*, 279–296. https://doi.org/10.1016/j.geomorph.2010.03.015

Larsen, L. G., Harvey, J. W., & Crimaldi, J. P. (2007). A delicate balance: Ecohydrological feedbacks governing landscape morphology in a lotic peatland. *Ecological Monographs*, *77*, 591–614. https://doi.org/10.1890/06-1267.1

Larsen, L. G., Ma, J., & Kaplan, D. (2017). How important is connectivity for surface water fluxes? A generalized expression for flow through heterogeneous landscapes. *Geophysical Research Letters*, *44*, 10,349–10,358. https://doi.org/10.1002/2017GL075432

Launder, B. E., & Spalding, D. B. (1974). The numerical computation of turbulent flows. *Computer Methods in Applied Mechanics and Engineering*, *3*, 269–289.

Lauzon, R., & Murray, A. B. (2018). Comparing the cohesive effects of mud and vegetation on delta evolution. *Geophysical Research Letters*, *45*, 10,437–10,445. https://doi.org/10.1029/2018GL079405

Le Hir, P., Monbet, Y., & Orvain, F. (2007). Sediment erodability in sediment transport modelling: Can we account for biota effects? *Continental Shelf Research*, *27*, 1116–1142. https://doi.org/10.1016/j.csr.2005.11.016

Licci, S., Nepf, H., Delolme, C., Marmonier, P., Bouma, T. J., & Puijalon, S. (2019). The role of patch size in ecosystem engineering capacity: A case study of aquatic vegetation. *Aquatic Sciences*, *81*, 41. https://doi.org/10.1007/s00027-019-0635-2

Marani, M., D'Alpaos, A., Lanzoni, S., Carniello, L., & Rinaldo, A. (2007). Biologically-controlled multiple equilibria of tidal landforms and the fate of the Venice lagoon. *Geophysical Research Letters*, *34*, L11402. https://doi.org/10.1029/2007GL030178

Mariotti, G. (2018). Marsh channel morphological response to sea level rise and sediment supply. *Estuarine, Coastal and Shelf Science*, *209*, 89–101. https://doi.org/10.1016/j.ecss.2018.05.016

Marjoribanks, T. I., Lague, D., Hardy, R. J., Boothroyd, R. J., Leroux, J., Mony, C., & Puijalon, S. (2019). Flexural rigidity and shoot reconfiguration determine wake length behind saltmarsh vegetation patches. *Journal of Geophysical Research: Earth Surface*, *124*, 2176–2196. https://doi.org/10.1029/2019JF005012

Meire, D. W. S. A., Kondziolka, J. M., & Nepf, H. M. (2014). Interaction between neighboring vegetation patches: Impact on flow and deposition. *Water Resources Research*, *50*, 3809–3825. https://doi.org/10.1002/2013WR015070

Morris, R. L., Konlechner, T. M., Ghisalberti, M., & Swearer, S. E. (2018). From grey to green: Efficacy of eco-engineering solutions for nature based coastal defence. *Global Change Biology*, *24*, 1827–1842. https://doi.org/10.1111/gcb.14063

Murray, A. B., Knaapen, M. A. F., Tal, M., & Kirwan, M. L. (2008). Biomorphodynamics: Physical biological feedbacks that shape landscapes. *Water Resources Research*, *44*, W11301. https://doi.org/10.1029/2007WR006410

Murray, A. B., & Paola, C. (2003). Modelling the effect of vegetation on channel pattern in bedload rivers. *Earth Surface Processes and Landforms*, *28*, 131–143. https://doi.org/10.1002/esp.428

Nakayama, T. (2012). Feedback and regime shift of mire ecosystem in northern Japan. *Hydrological Processes*, *26*, 2455–2469. https://doi.org/10.1002/hyp.9347

Narayan, S., Beck, M. W., Reguero, B. G., Losada, I. J., van Wesenbeeck, B., Pontee, N., et al. (2016). The effectiveness, costs and coastal protection benefits of natural and nature-based defences. *PLOS ONE*, *11*(5), e0154735. https://doi.org/10.1371/journal.pone.0154735

Nepf, H. M. (2012). Hydrodynamics of vegetated channels. *Journal of Hydraulic Research*, *50*, 262–279. https://doi.org/10.1080/00221686.2012.696559

Ortiz, A. C., Ashton, A., & Nepf, H. (2013). Mean and turbulent velocity fields near rigid and flexible plants and the implications for deposition. *Journal of Geophysical Research: Earth Surface*, *118*, 2585–2599. https://doi.org/10.1002/2013JF002858
Partheniades, E. (1965). Erosion and deposition of cohesive soils. *Journal of the Hydraulics Division*, *91*, 105–139.
Piliouras, A., & Kim, W. (2019). Upstream and downstream boundary conditions control the physical and biological development of river deltas. *Geophysical Research Letters*, *46*, 11,188–11,196. https://doi.org/10.1029/2019GL084045
Reinhardt, L., Jerolmack, D., Cardinale, B. J., Vanacker, V., & Wright, J. (2010). Dynamic interactions of life and its landscape: Feedbacks at the interface of geomorphology and ecology. *Earth Surface Processes and Landforms*, *35*, 78–101. https://doi.org/10.1002/esp.1912
Rietkerk, M., Dekker, S. C., Wassen, M. J., Verkroost, A. W. M., & Bierkens, M. F. P. (2004). A putative mechanism for bog patterning. *The American Naturalist*, *163*, 699–708. https://doi.org/10.1086/383065
Saco, P. M., Willgoose, G. R., & Hancock, G. R. (2007). Eco-geomorphology of banded vegetation patterns in arid and semi-arid regions. *Hydrology and Earth System Sciences*, *11*, 1717–1730. https://doi.org/10.5194/hess-11-1717-2007
Sandi, S. G., Rodrguez, J. F., Saintilan, N., Riccardi, G., & Saco, P. M. (2018). Rising tides, rising gates: The complex ecogeomorphic response of coastal wetlands to sea-level rise and human interventions. *Advances in Water Resources*, *114*, 135–148. https://doi.org/10.1016/j.advwatres.2018.02.006
Sanford, L. P., & Halka, J. P. (1993). Assessing the paradigm of mutually exclusive erosion and deposition of mud, with examples from upper Chesapeake Bay. *Marine Geology*, *114*, 37–57.
Schoelynck, J., Groote, T., Bal, K., Vandenbruwaene, W., Meire, P., & Temmerman, S. (2012). Self organised patchiness and scale dependent biogeomorphic feedbacks in aquatic river vegetation. *Ecography*, *35*, 760–768. https://doi.org/10.1111/j.1600-0587.2011.07177.x
Schwarz, C., Bouma, T. J., Zhang, L. Q., Temmerman, S., Ysebaert, T., & Herman, P. M. J. (2015). Interactions between plant traits and sediment characteristics influencing species establishment and scale-dependent feedbacks in salt marsh ecosystems. *Geomorphology*, *250*, 298–307. https://doi.org/10.1016/j.geomorph.2015.09.013
Schwarz, C., Gourgue, O., van Belzen, J., Zhu, Z., Bouma, T. J., van de Koppel, J., et al. (2018). Self-organization of a biogeomorphic landscape controlled by plant life-history traits. *Nature Geoscience*, *11*, 672–677. https://doi.org/10.1038/s41561-018-0180-y
Schwarz, C., Ye, Q. H., Van der Wal, D., Zhang, L. Q., Bouma, T., Ysebaert, T., & Herman, P. M. J. (2014). Impacts of salt marsh plants on tidal channel initiation and inheritance. *Journal of Geophysical Research: Earth Surface*, *119*, 385–400. https://doi.org/10.1002/2013JF002900
Solari, L., Van Oorschot, M., Belletti, B., Hendriks, D., Rinaldi, M., & Vargas-Luna, A. (2016). Advances on modelling riparian vegetation-hydromorphology interactions. *River Research and Applications*, *32*, 164–178. https://doi.org/10.1002/rra.2910
Taramelli, A., Valentini, E., Cornacchia, L., Monbaliu, J., & Sabbe, K. (2018). Indications of dynamic effects on scaling relationships between channel sinuosity and vegetation patch size across a salt marsh platform. *Journal of Geophysical Research: Earth Surface*, *123*, 2714–2731. https://doi.org/10.1029/2017JF004540
Taylor, K. E. (2001). Summarizing multiple aspects of model performance in a single diagram. *Journal of Geophysical Research*, *106*, 7183–7192. https://doi.org/10.1029/2000JD900719
Temmerman, S., Bouma, T. J., van de Koppel, J., Van der Wal, D., De Vries, M. B., & Herman, P. M. J. (2007). Vegetation causes channel erosion in a tidal landscape. *Geology*, *35*, 631–634. https://doi.org/10.1130/g23502a.1
Temmerman, S., & Kirwan, M. L. (2015). Building land with a rising sea. *Science*, *349*, 588–589. https://doi.org/10.1126/science.aac8312
Thorslund, J., Jarsjo, J., Jaramillo, F., Jawitz, J. W., Manzoni, S., Basu, N. B., et al. (2017). Wetlands as large-scale nature-based solutions: Status and challenges for research, engineering and management. *Ecological Engineering*, *108*, 489–497. https://doi.org/10.1016/j.ecoleng.2017.07.012
Van Coppenolle, R., & Temmerman, S. (2020). Identifying global hotspots where coastal wetland conservation can contribute to nature-based mitigation of coastal flood risks. *Global and Planetary Change*, *187*, 103,125. https://doi.org/10.1016/j.gloplacha.2020.103125
van Wesenbeeck, B. K., Mulder, J. P. M., Marchand, M., Reed, D. J., de Vries, M. B., de Vriend, H. J., & Herman, P. M. J. (2014). Damming deltas: A practice of the past? Towards nature-based flood defenses. *Estuarine, Coastal and Shelf Science*, *140*, 1–6. https://doi.org/10.1016/j.ecss.2013.12.031
van Wesenbeeck, B. K., van de Koppel, J., Herman, P. M. J., & Bouma, T. J. (2008). Does scale dependent feedback explain spatial complexity in salt marsh ecosystems? *Oikos*, *117*, 152–159. https://doi.org/10.1111/j.2007.0030-1299.16245.x
van de Koppel, J., Bouma, T. J., & Herman, P. M. J. (2012). The influence of local-and landscape-scale processes on spatial self-organization in estuarine ecosystems. *Journal of Experimental Biology*, *215*, 962–967. https://doi.org/10.1242/jeb.060467
van de Vijsel, R. C., van Belzen, J., Bouma, T. J., van der Wal, D., Cusseddu, V., Purkis, S. J., et al. (2020). Estuarine biofilm patterns: Modern analogues for Precambrian self organization. *Earth Surface Processes and Landforms*, *45*, 1141–1154. https://doi.org/10.1002/esp.4783
van der Heide, T., Bouma, T. J., van Nes, E. H., van de Koppel, J., Scheffer, M., Roelofs, J. G. M., et al. (2010). Spatial self organized patterning in seagrasses along a depth gradient of an intertidal ecosystem. *Ecology*, *91*, 362–369. https://doi.org/10.1890/08-1567.1
Van der Wal, D., Wielemaker-Van den Dool, A., & Herman, P. M. J. (2008). Spatial patterns, rates and mechanisms of saltmarsh cycles (Westerschelde, the Netherlands). *Estuarine, Coastal and Shelf Science*, *76*, 357–368. https://doi.org/10.1016/j.ecss.2007.07.017
Vandenbruwaene, W., Schwarz, C., Bouma, T. J., Meire, P., & Temmerman, S. (2015). Landscape-scale flow patterns over a vegetated tidal marsh and an unvegetated tidal flat: Implications for the landform properties of the intertidal floodplain. *Geomorphology*, *231*, 40–52. https://doi.org/10.1016/j.geomorph.2014.11.020
Vandenbruwaene, W., Temmerman, S., Bouma, T. J., Klaassen, P. C., De Vries, M. B., Callaghan, D. P., et al. (2011). Flow interaction with dynamic vegetation patches: Implications for biogeomorphic evolution of a tidal landscape. *Journal of Geophysical Research*, *116*, F01008. https://doi.org/10.1029/2006JF000537
Virtanen, P., Gommers, R., Oliphant, T. E., Haberland, M., Reddy, T., Cournapeau, D., et al. (2019). SciPy 1.0–Fundamental algorithms for scientific computing in Python. arXiv e-prints. https://doi.org/10.1038/s41592-019-0686-2
Vogel, S. (1996). *Life in moving fluids: The physical biology of flow* (second edition). Princeton: Princeton University Press. ISBN: 9780691026169
Volp, N. D., Prooijen, B. C., & Stelling, G. S. (2013). A finite volume approach for shallow water flow accounting for high resolution bathymetry and roughness data. *Coastal Engineering*, *49*, 4126–4135. https://doi.org/10.1002/wrcr.20324
Vuik, V., Jonkman, S. N., Borsje, B. W., & Suzuki, T. (2016). Nature-based flood protection: The efficiency of vegetated foreshores for reducing wave loads on coastal dikes. *Coastal Engineering*, *116*, 42–56. https://doi.org/10.1016/j.coastaleng.2016.06.001
Winterwerp, J. C. (2007). On the sedimentation rate of cohesive sediment. In J. P.-Y. Maa, L. P. Sanford, D. H. Schoellhamer (Eds.), *Estuarine and coastal fine sediments dynamics, Proceedings in Marine Science* (Vol. 8, pp. 209–226). The Netherlands: Elsevier.
Wright, K., Hiatt, M., & Passalacqua, P. (2018). Hydrological connectivity in vegetated river deltas: The importance of patchiness below a threshold. *Geophysical Research Letters*, *45*, 10,416–10,427. https://doi.org/10.1029/2018GL079183

Wu, G., Shi, F., Kirby, J. T., Mieras, R., Liang, B., Li, H., & Shi, J. (2016). A pre-storage, subgrid model for simulating flooding and draining processes in salt marshes. *Coastal Engineering*, *108*, 65–78. https://doi.org/10.1016/j.coastaleng.2015.11.008

Yamasaki, T. N., Lima, P. H. S., Silva, D. F., Preza, C. G. A., Janzen, J. G., & Nepf, H. M. (2019). From patch to channel scale: The evolution of emergent vegetation in a channel. *Advances in Water Resources*, *129*, 131–145. https://doi.org/10.1016/j.advwatres.2019.05.009

Zhang, X., Leonardi, N., Donatelli, C., & Fagherazzi, S. (2019). Fate of cohesive sediments in a marsh-dominated estuary. *Advances in Water Resources*, *125*, 32–40. https://doi.org/10.1016/j.advwatres.2019.01.003

Zhou, Z., Ye, Q., & Coco, G. (2016). A one-dimensional biomorphodynamic model of tidal flats: Sediment sorting, marsh distribution, and carbon accumulation under sea level rise. *Advances in Water Resources*, *93*, 288–302. https://doi.org/10.1016/j.advwatres.2015.10.011

Zong, L., & Nepf, H. (2010). Flow and deposition in and around a finite patch of vegetation. *Geomorphology*, *116*, 363–372. https://doi.org/10.1016/j.geomorph.2009.11.020